ISSN 1991-1696

Africa Research Journal

Research Journal of the South African Institute of Electrical Engineers

Incorporating the SAIEE Transactions

SAIEE AFRICA RESEARCH JOURNAL Vol 100 No.1 pp 1-32

www.saiee.org.za

March 2009
Volume 100 No. 1

SAIEE AFRICA RESEARCH JOURNAL

(SAIEE FOUNDED JUNE 1909 INCORPORATED DECEMBER 1909)
AN OFFICIAL JOURNAL OF THE INSTITUTE
ISSN 1991-1696

Secretary and Head Office
Ms Gerda Geyer
South African Institute for Electrical Engineers (SAIEE)
PO Box 751253, Gardenview, 2047, South Africa
Tel: (27-11) 487-3003
Fax: (27-11) 487-3002
E-mail: geyerg@saiee.org.za

Published by
SAIEE Publications (Pty) Ltd, PO Box 751253, Gardenview, 2047,
Tel. (27-11) 487-3003, Fax. (27-11) 487-3002,
E-mail: SAIEEPublications@saiee.org.za

Additional reviewers are approached as necessary
ARTICLES SUBMITTED TO THE SAIEE AFRICA RESEARCH JOURNAL ARE FULLY PEER REVIEWED
PRIOR TO ACCEPTANCE FOR PUBLICATION

The following organizations have listed SAIEE Africa Research Journal for abstraction purposes:
INSPEC (The Institution of Electrical Engineers, London); "The Engineering Index" (Engineering Information Inc.)

SAIEE AFRICA RESEARCH JOURNAL – NOTES FOR AUTHORS

This journal publishes research, survey and expository contributions in the field of electrical, electronics, computer, information and communications engineering. Articles may be of a theoretical or applied nature, must be novel and must not have been published elsewhere.

Nature of Articles

Two types of articles may be submitted:

- Papers: Presentation of significant research and development and/or novel applications in electrical, electronic, computer, information or communications engineering.
- Research and Development Notes: Brief technical contributions, technical comments on published papers or on electrical engineering topics.

All contributions are reviewed with the aid of appropriate reviewers. A slightly simplified review procedure is used in the case of Research and Development Notes, to minimize publication delays. No maximum length for a paper is prescribed. However, authors should keep in mind that a significant factor in the review of the manuscript will be its length relative to its content and clarity of writing. Membership of the SAIEE is not required.

Process for initial submission of manuscript

Preferred submission is by e-mail in electronic MS Word and PDF formats. PDF format files should be 'press optimised' and include all embedded fonts, diagrams etc. All diagrams to be in black and white (not colour). For printed submissions contact the Managing Editor. Submissions should be made to:

The Managing Editor, SAIEE Africa Research Journal,
PO Box 751253, Gardenview 2047, South Africa.
E-mail: researchjournal@saiee.org.za

These submissions will be used in the review process. Receipt will be acknowledged by the Editor-in-Chief and subsequently by the assigned Specialist Editor, who will further handle the paper and all correspondence pertaining to it. Once accepted for publication, you will be notified of acceptance and of any alterations necessary. You will then be requested to prepare and submit the final script. The initial paper should be structured as follows:

- TITLE in capitals, not underlined.
- Author name(s): First name(s) or initials, surname (without academic title or preposition 'by')
- Abstract, in single spacing, not exceeding 20 lines.
- Text in 1½ spacing.
- List of references (references to published literature should be cited in the text using Arabian numerals in square brackets and arranged in numerical order in the List of References).
- Author(s) affiliation and postal address(es).
- Footnotes, if unavoidable, should be typed in single spacing.

Format of the final manuscript

The final manuscript will be produced in a 'direct to plate' process. The assigned Specialist Editor will provide you with instructions for preparation of the final manuscript and required format, to be submitted directly to:
The Managing Editor, SAIEE Africa Research Journal, PO Box 751253, Gardenview 2047, South Africa.
E-mail: researchjournal@saiee.org.za

Page charges

A page charge of R200 per page will be charged to offset some of the expenses incurred in publishing the work. Detailed instructions will be sent to you once your manuscript has been accepted for publication.

Additional copies

An additional copy of the issue in which articles appear, will be provided free of charge to authors.
If the page charge is honoured the authors will also receive 10 free reprints without covers.

Copyright

Unless otherwise stated on the first page of a published paper, copyright in all contributions accepted for publication is vested in the SAIEE, from whom permission should be obtained for the publication of whole or part of such material.

Website: www.saiee.org.za/arj

VOL 100 No 1
March 2009

SAIEE Africa Research Journal

COMPARISON OF FEATURES RESPONSE IN TEXTURE-BASED IRIS SEGMENTATION

Asheer Bachoo* **and Jules-Raymond Tapamo****

* *Optronic Sensor Systems, Defence Peace Safety and Security, Council of Scientific and Industrial Research, Pretoria, 0001, South Africa*
Email: abachoo@csir.co.za

** *School of Computer Science, University of Kwazulu-Natal, Durban, 4000, South Africa*
Email: tapamoj@ukzn.ac.za

Abstract: Identification of individuals using iris recognition is an emerging technology. Segmentation of the iris texture from an acquired digital image of the eye is not always accurate - the image contains noise elements such as skin, reflection and eyelashes that corrupt the iris region of interest. An accurate segmentation algorithm must localize and remove these noise components. Texture features are considered in this paper for describing iris and non-iris regions. These regions are classified using the Fisher linear discriminant and the iris region of interest is extracted. Four texture description methods are compared for segmenting iris texture using a region based pattern classification approach: Grey Level Co-occurrence Matrix (GLCM), Discrete Wavelet Transform (DWT), Gabor Filters (GABOR) and Markov Random Fields (MRF). These techniques are evaluated according to their true and false classifications for iris and non-iris pixels.

Keywords: iris, texture features, segmentation, pattern classification

1. INTRODUCTION

The iris [1] begins its formation in the 3rd month of gestation. It is a multilayered texture and an assortment of variations are possible. They include contractile lines related to the state of the pupil, irregular atrophy of the border layer (crypts), small elevations of the border layer (naevi), collections of chromatophores (freckles) and color variation.
Segmentation of an iris image is a classical image processing problem. The following occurrences are possible in the acquired iris image:

- Bright lighting can cause specular reflection off the eye, which makes the processing stage almost impossible at times.
- Poor lighting can hide the textural details and introduce an uneven illumination component.
- Atmospheric conditions and human emotion affect the state and size of the pupil. This causes the iris region to vary in size.
- The iris may be partially hidden. This can be caused by eyelashes and eyelids.

The focus of this research paper is to improve the iris segmentation process by considering the above image components as a normal occurrence in an iris image. The iris region that must be extracted has texture properties that are *different* from those of pixels of eyelashes, reflection, pupil and eyelids. This provides the basis for a texture feature extraction and pattern classification approach for segmenting the different components from the iris image. We compare four texture description methods for iris segmentation: grey level co-occurrence matrix, discrete wavelet transform, Gabor filters and Markov random fields.

Several approaches are documented that account for poor or corrupted iris texture. Eyelash and reflection detection has been proposed by Kong and Zhang [2]. They divide the eyelash problem into two possibilities: separable eyelashes and multiple eyelashes. Separable eyelashes are treated as edges whereas multiple eyelashes are modelled using an intensity variation model - eyelashes overlapping in a small area have a low intensity variation. If the variance of intensity in the area is below a threshold, the center of the window is labelled an eyelash pixel. Reflections are defined as strong and weak. A pixel of strong reflection has an intensity value greater than a specified threshold; a pixel of weak reflection is a transition region between strong reflection and the iris. The approach described above is effective. However, there is a use of thresholding for determining eyelash pixels and the threshold is not automatically determined. If the region being thresholded does not have two distinct grey level distributions - corresponding to iris and eyelash pixels - the algorithm may fail. Incorrect threshold selection will also affect the result negatively.

In the work of Huang *et. al.* [3], occlusion by eyelids, eyelashes and specular reflection is considered. Edge data is extracted using phase congruency information and this is then used to determine the most likely boundaries of noise and/or occlusion. The frequency distribution of

iris images has been analyzed to determine occlusions by eyelids and eyelashes [4]. Frequencies in the Fourier domain provide an insight into the content of the iris region - frequencies outside a specified range signify occlusion by eyelids and/or eyelashes. This enables the system to accept or reject an image for processing. Although effective, the technique does not provide a solution to removing the useless regions. In the next section, the methods implemented are discussed.

2. METHODS

The proposed algorithm for segmenting iris images has several important steps. Firstly, an iris image is provided as input to the system and the iris boundaries are located. Therafter, the located iris region is normalized using a transform that makes it invariant to size. The normalized image also has its contrast enhanced. Texture features are then computed for the normalized iris region. These features are either used to train a classifier or segment the normalized iris region i.e. remove noise components. The images processed during this investigation were taken from the *CASIA Iris Database* and are 8-bit grey scale [5]. This database is available from the National Laboratory of Pattern Recognition, Chinese Academy of Sciences.

2.1 Iris boundary localization

The inner and outer iris contours are located by modelling them as circles and the eyelids are modelled using parabolic arcs. This proceeds as follows:

1. The input image is globally thresholded using an empirically determined grey scale value of 70. This step segments most of the pupil and provides a binary image. Canny edge detection is applied on the binarized image and an edge map is generated [6]. The pupil is then localized by an application of the Hough transform on the edge map for circle detection [7].

2. The input image is processed in a second pass during which greyscale opening and closing is performed. This processing has the effect of reducing the noise presented by eyelashes and reflection. Thereafter, the image contrast is enhanced by linearly stretching its histogram. An edge map is then generated from the enhanced image using the Canny edge detector and this data is fed to the Hough transform described above. The position of the localized pupil is used as a reference point for finding the center of the circle that lies on the outer iris boundary.

3. The edge map generated in the above step is then processed by a least squares algorithm that fits parabolic arcs to the eyelids. The RANSAC algorithm is incorporated into this process in order to minimize the effect of outliers [8]. The circle parameters are used to reduce the search space for eyelid points and to help differentiate between upper and lower eyelids.

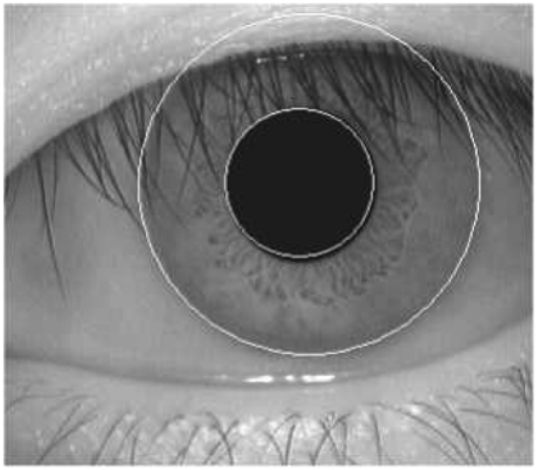

(a) Input iris image with located boundaries

(b) Normalized iris region with eyelids masked out

Figure 1: Iris image pre-processing

The parabolic boundaries computed in the above steps are used to mask out the eyelid pixels when texture analysis is performed.

2.2 Iris normalization

Daugman's rubber sheet model is used to transform the extracted iris region to a dimensionless polar coordinate system [9]. The normalized image is a rectangular grid of size 544×96 pixels. This ensures continuity of texture pixels and also allows fast execution of the discrete wavelet transform. Eyelid regions are then masked out using the parabolas fitted to the eyelid boundaries. Uneven illumination in the iris image causes discontinuities that break up objects when segmentation is performed. It may also degrade object and texture details, making different objects appear the same. The opposite can also occur - similar objects can appear very different. As a result, the multi-scale Retinex [10] is used for illumination flattening before contrast enhancement is performed by histogram adjustment [11]. Figure 1(a) shows an input iris image with its boundaries located. Figure 1(b) is the normalized iris region with the eyelids removed.

2.3 Texture segmentation

In real world problems, images do not demonstrate uniform intensities - they contain variations in tonal content. This represents the textures in the image and their parameters are estimated during the processing stage.

These parameters give texture primitives varying degrees of fineness, coarseness and periodicity of patterns. There is no universal definition of texture since definitions are related to the method of analysis [12]. Texture can be described in terms of texture strength. Strong texture has well defined primitives with a regular structure - elements and spatial relations are easily determined. Weak textures have primitives and spatial relations that are difficult to define - they are referred to as random [13]. It can be regarded as a grouping of similarity in the image [14]; a repetition of basic structural patterns [15]; or as intensity variations that follow a particular periodicity [16]. Once localization and normalization of an iris region has been performed, texture features are computed for the region pixels. These features are filtered using local averaging. This establishes a set of region properties for each pixel. Thereafter, pixels with similar properties are merged into regions and these regions are classified using pattern classification. A brief description of the implemented texture analysis techniques follows.

Grey Level Co-occurrence Matrix (GLCM): Discriminating features for texture separation can be computed using the statistical approach of grey level co-occurrence matrices [17,18]. A GLCM is a matrix of second order statistics that represents pixel configurations as probabilities of pairwise grey level occurrences. These pairwise occurrences must satisfy a particular relationship in order to contribute to the probability matrix. The pixel-pair relationship denotes a spatial dependency for a particular texture. These dependencies are observed in the GLCM, from which a number of features can be computed. This approach has been found to be very popular and effective [19–22].
Considering an $N \times N$ window in a textured image, the configuration of gray-levels can be represented by the matrix $P_{\theta,d}(i,j)$ describing how frequently two pixels with gray-levels i, j appear in the window separated by a distance d in the direction θ [13]. From $P_{\theta,d}$ several Haralick texture features can be extracted, among which some have been used for our experiments [17, 18]. They are:

$$\text{CONT} = \sum_{i,j=1}^{N} (i-j)^2 p_{\theta,d}(i,j) \tag{1}$$

$$\text{ENTR} = -\sum_{i,j=1}^{N} p_{\theta,d}(i,j) \log p_{\theta,d}(i,j) \tag{2}$$

$$\text{MEAN}_1 = \mu = \mu_x = \sum_{i,j=1}^{N} i P_x(i,j) \tag{3}$$

$$\text{SDEV} = \sqrt{\sum_{i,j=1}^{N} P_x(i,j)(i-\mu)^2} \tag{4}$$

where

$$P_x(i) = \sum_{j=1}^{N} p_{\theta,d}(i,j) \tag{5}$$

The features above are the contrast (CONT), entropy (ENTR), mean (MEAN_1) and standard deviation (SDEV) of the GLCM. These features were selected by considering the guidelines presented in [23]. For computational efficiency and improved co-occurrence relations of pixels, we reduce the number of grey levels in the input image to 32. This is done using a straight forward linear scaling. We use $\theta \in \{0, 45, 90, 135\}$, $d \in \{1\}$ and a 9×9 window for computing GLCMs. These parameters produce 16 features for each pixel in the input image.

Discrete Wavelet Transform (DWT): Wavelets are multi-scale transforms that can be used to characterize texture [24]. They provide information about the frequency content of an image. In our context, the DWT applies Haar wavelets to decompose images into Low-Low (LL), Low-High (LH), High-Low (HL) and High-High (HH) frequency components.
The DWT is applied to a 2D digital image $f(x,y)$ by filtering across the rows and then the columns of the result [25, 26]. This is followed by downsampling by a factor 2 to achieve the effect of scaling. The filtering process produces detail (d_j) and approximation (a_j) coefficients at scale j. Processing for the next level ($j+1$) consists of using the a_j as the input. These are the high and low frequency components respectively. The filtering and downsampling operations can be represented using 2×2 kernels which correspond to different frequency components e.g. High-High or Low-High. Convolving every 2×2 non-overlapping block of pixels produces a result equivalent to applying a set of filters across the rows and columns and then downsampling. Kernels for a generalized Haar transform are shown in Figure 2.
Features computed are:

$$\text{MEAN}_2 = \frac{1}{N^2} \sum_{i=1}^{N} d(i)_j \tag{6}$$

$$\text{AAD}_1 = \frac{1}{N^2} \sum_{i=1} \mid d(i)_j - \text{MEAN}_2 \mid \tag{7}$$

$$\text{ENER}_1 = \frac{1}{N^2} \sum_{i=1}^{N} [d(i)_j]^2 \tag{8}$$

where $d(i)$ is a detail coefficient at level j and N is the number of coefficients at level j. ENER measures the signal energy - high energies correspond to high frequency variations. It measures variations in texture patterns at different resolutions. AAD_1 measures the dispersion of coefficients around the mean. MEAN_2 is the common statistical property of a set of samples.
A generalized Haar algorithm decomposes the image, extracting detail and approximation coefficients [24,27]. To perform feature extraction, a 8×8 window is centered at each pixel and 2 passes of the Haar algorithm is performed on windowed pixels together with computation of the statistical information. At each scale, 4 sub-images are produced from the detail and approximation coefficients -

1	1	-1	-1	-1	1	1	-1
1	1	1	1	-1	1	-1	1

Figure 2: Haar kernels operators LL, LH, HL, HH

LL, LH, HL and HH. Features are computed for LL, LH and HL. For LL, the MEAN_2 and AAD_1 are computed. For LH and HL, ENER_1 is computed. Thus, for each pass, 4 features are computed. In addition, the MEAN_2 and AAD_1 are computed for the original image. This provides a total of 10 features for the DWT transform of a texture.

Gabor Filters (GABOR): A popular method for texture feature extraction is the multi-channel filtering approach using Gabor filters [28–30]. This technique is able to exhibit some characteristics of the human visual system. It uses a multi-resolution system to extract information that describes different characteristics of an image. An image is convolved with a set of filters and the outputs are processed to establish a set of texture properties for a pixel.
The Gabor function implemented has the following form:

$$g(x,y) = exp\{-\frac{1}{2}(\frac{x^2}{{\sigma_x}^2} + \frac{y^2}{{\sigma_y}^2})\}cos(\frac{2\pi}{\lambda} + \phi) \quad (9)$$

where:

$$\sigma_x = \frac{\sqrt{ln2}(2^{B_f}+1)}{\frac{\sqrt{2}\pi}{\lambda}(2^{B_f}-1)} \quad (10)$$

$$\sigma_y = \frac{\sqrt{ln2}}{\frac{\sqrt{2}\pi}{\lambda}tan(\frac{B_\theta}{2})} \quad (11)$$

Frequency of the sinusoids is denoted $\frac{1}{\lambda}$. The spread of the Gaussian in the x and y directions is controlled by σ_x and σ_y respectively. The frequency bandwidth of the filter is represented by B_f, the angular bandwidth by B_θ and the phase is ϕ. Spatial rotation of the filter by θ degrees can be achieved using:

$$x^{'} = x\cos\theta + y\sin\theta \quad (12)$$

$$y^{'} = -x\sin\theta + y\cos\theta \quad (13)$$

and then substituting these new values for x and y.
The Gabor kernels require a number of parameters for computation. The value for B_f is set to 1 (octave) and B_θ is 30 degrees [31]. Given a set of λs, the corresponding σs can be determined from the σ:λ ratio. The application dependent parameters are λ, θ, ϕ and γ. γ is set to 0.5 and $\theta \in \{0°, 30°, 60°, 90°, 120°, 150°\}$. The values for λ are $\{1.41, 2.82\}$. ϕ should be set to 0 for creating a symmetric filter or $-\frac{\pi}{2}$ for an anti-symmetric filter. These parameters were determined from empirical results.
The filtering produces feature images and the data in these images can be used directly as features for texture discrimination. In addition, each feature image F_k can be processed further for feature extraction. The following features can be derived for a point in F_k centered within a square window of width W

$$\text{ENER}_2 = \frac{1}{N}\sum_{x,y\in W}\sqrt{[F_k^{odd}(x,y)]^2 + [F_k^{even}(x,y)]^2} \quad (14)$$

where N is the number of points in the region W. F_k^{odd} and F_k^{even} refer to anti-symmetric and symmetric filter reponses respectively. The literature suggests using Gaussian weighted windows in the above computation [32, 33]. We use a Guassian with spatial extent 1.3 times larger than the Gabor wavelength.

Markov Random Fields (MRF): A Markov random field texture model represents the global intensity distribution of an image as the joint probability distribution of local conditional systems of each pixel in the image. The image intensity pixel depends only on a set of neighbourhood pixels.
In order to model a texture region using MRFs the Markov process, for a pixel c in image X, is described by a symmetric difference equation [34]:

$$X(c) = \sum \beta_{c,m}[X(c+m) + X(c-m)] + e_c \quad (15)$$

where e_c is a zero mean Gaussian distributed noise (estimation error), m is an offset from the center cell c and $\beta_{c,m}$ are parameters that weigh a pair of symmetric neighbours to the center cell. The βs form the features vector that describes the Markovian properties of the texture and govern the spatial interactions. A region R of size $w \times w$ is defined together with the order of the neighbourhood. The order describes the set of pairs of symmetrical neighbours, and their offsets m from center pixel c, that interact with the center pixel. For every pixel c in R, its neighbouring pixels up to the specified order describe a spatial interaction with the pixel. These spatial interactions for all c in R are modelled using the Gauss model described above. We can represent Eq. (15) in matrix notation:

$$X(c) = \beta^T Q_c + e_c \quad (16)$$

where β^T is a vector consisting of all the $\beta_{c,m}$ and Q_c is a vector defined by:

$$Q_c = \begin{bmatrix} X(c+m_1) + X(c-m_1) \\ X(c+m_2) + X(c-m_2) \\ X(c+m_3) + X(c-m_3) \\ \cdots \end{bmatrix} \quad (17)$$

The βs are estimated using a least squares approach. Features for a region R are computed by a modified method based on the one presented by Cesmeli and Wang [35]:

$$\mathrm{AAD}_2 = \frac{1}{w^2} \sum_{c \in R} \mid X(c) - \beta_j Q_{c_j} \mid \qquad (18)$$

where w^2 is the number of points in R. The neighbourhood order is 2, which has 4 pairs of symmetric neighbours. Hence, the number of texture features is 4. The region R is 9×9 in size.

Parameter estimation and features extraction: The choice of parameters for texture description is important for accurate image segmentation. Parameters for the implemented methods are estimated empirically. The feature images produced from the feature extraction process are filtered (using local averaging of a 5×5 window) to remove sharp spikes. Texture features are normalized so that the sample distribution for each image has zero mean and unit variance. Table 1 summarizes the texture description parameters.

Region merging: Clustering is used to group similar pixels together based on their computed texture features. This creates homogenous regions in an image that can be segmented. Fuzzy clustering allows data to belong to more than one class [36, 37]. This is reflected by their degree of membership in a particular cluster. It is based on the minimization of the objective function

$$J_m = \sum_{j=1}^{C} \sum_{i=1}^{N} u_{ij}^m \parallel \mathbf{x}_i - \mathbf{c}_i \parallel^2 \ , 1 \leq m \leq \infty \qquad (19)$$

where m, the fuzzy factor, is a real number greater than 1, u_{ij} the degree of membership of $\mathbf{x}_i$ in the cluster j and $\mathbf{x}_i$ is the ith d-dimensional data. The d-dimensional center of a cluster is denoted by $\mathbf{c}_j$ and $\parallel * \parallel$ is the norm. The variables C and N refer to the number of clusters and the number of members per cluster respectively.
Fuzzy partitioning is an iterative optimization process. The membership u_{ij}, in matrix U, and the cluster centers $\mathbf{c}_j$ are computed by

$$u_{ij} = \frac{1}{\sum_{k=1}^{C} (\frac{\|\mathbf{x}_i - \mathbf{c}_j\|}{\|\mathbf{x}_i - \mathbf{c}_j\|})^{\frac{2}{m-1}}} \qquad (20)$$

$$\mathbf{c}_j = \frac{\sum_{i=1}^{N} u_{ij}^m \cdot \mathbf{x}_i}{\sum_{i=1}^{N} u_{ij}^m} \qquad (21)$$

The algorithm terminates when $\mid u_{ij}^{k+1} - u_{ij}^k \mid$ is less than ϵ, where ϵ is a threshold between 0 and 1 and k an iteration step.

Classifier design: The segmentation algorithm that is implemented uses supervised classification to identify image regions created by the fuzzy clustering algorithm. A training phase incorporates *a priori* knowledge into a classifier. Ideally, the training images will effectively represent the structure of the feature space of unknown samples. A common issue in supervised classifier design is the presence of a large number of pattern samples that make the training process extremely inefficient. We first perform sample selection before computing classifier parameters.

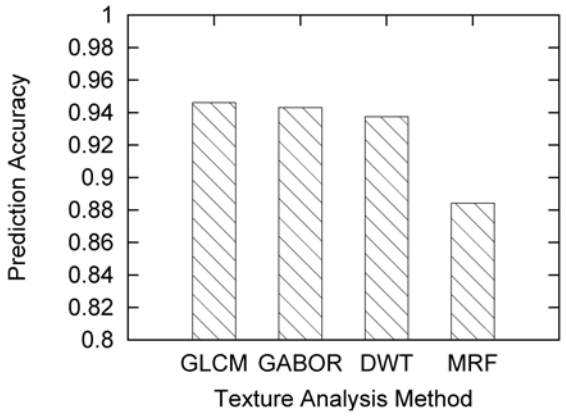

Figure 3: Average prediction accuracy

20 images are selected for training samples. In these images, the different image regions are labelled, denoted as IRIS, PUPIL, REFLECTION, SKIN and EYELASH. The labelled image and the original image form the input to an algorithm that computes texture features and then uses the labelled image to construct sets of feature vectors belonging to the image regions mentioned above. These pattern sets are then reduced separately, recombined and evaluated for information content.

A sample set f is reduced by removing redundant samples using a KNN algorithm [38]. A k value is first specified and then the algorithm proceeds by selecting a pattern $\mathbf{x}$ from f and discarding its k nearest neighbours in f. The selected feature vector is placed in a new set f_{new}. The initial set f will now contain neither $\mathbf{x}$ nor its k nearest neighbours. This process is repeated on f until it is empty. From an empirical evaluation, we use $k = 20$ which selects approximately 2500 vectors (about 5% of the total feature set in the image) - this eases the computational burden and also reduces the risk of overtraining. The information content of the selected samples is measured by considering their ability to predict labels of the initial sample set.

Given an unlabelled image pixel and its feature vector from the initial sample set, we assign to the pixel the label of the vector in the reduced set that is nearest to it (the Euclidean distance is used for feature comparison). The predicted labels are then compared to the actual class labels and a normalized prediction accuracy is computed - 1 denotes the ability to predict all labels correctly; 0 denotes no labels being predicted correctly at all.

Figure 3 shows the average predication accuracy for the 20 training images. The accuracies for the GLCM, GABOR and DWT methods are similar. However, the MRF accuracy is significantly lower. This highlights

Table 1: Summary of texture parameters

Method	Parameters	Features	Window size	#Features
GLCM	$\theta \in \{0°, 45°, 90°, 135°\}$ $d \in \{1\}$	CONT, ENTR $MEAN_1$, SDEV	9×9	16
DWT	2 passes	Original image - $MEAN_2$, AAD_1 Each pass - LL: $MEAN_2$, AAD_1 LH, HL: $ENER_1$	8×8	10
GABOR	$\gamma = 0.5, B_f = 1.0, B_\theta = 30°$ $\theta \in \{0°, 30°, 60°, 90°, 120°, 150°\}$ $\lambda \in \{1.41, 2.82\}$	$ENER_2$	Dependent on λ	12
MRF	Order=2	AAD_2	9×9	4

the fact that more samples are required, as compared to the other methods, to effectively represent its pattern set. Since we are using a KNN approach to remove redundant samples, we can conclude that the feature vectors of the GLCM, GABOR and DWT are generally more compact than the MRF. The KNN algorithm will retain important information if clusters are compact since a selected feature vector has had neighbours discarded that are very close to it in feature space. In the case of the MRF, a pattern not similar to the selected one but included in the set of *k* nearest neighbours will be discarded. Compactness is highly desirable for homogeneity. Our method of subset selection of samples provides a good estimate of the original feature space since 88 to 95% of the patterns can be correctly predicted for the different texture analysis methods. The selected samples are used to estimate parameters for the classifier.

A classifier that uses the 2 class Fisher linear discriminant is implemented for region classification [11]. The selected sample sets for the 20 training images and their corresponding labels are used to compute a discriminant for every combination of two classes (producing 10 discriminants). This is done for each texture method to complete the learning process. Given the five image region classes (IRIS, PUPIL, REFLECTION, SKIN and EYELASH) we have 10 two category combinations e.g. IRIS-EYELASH, REFLECTION-PUPIL, etc. For each pair of categories, the Fisher method computes a weight vector **w** for the separating plane. As such, an *n*-dimensional sample is projected to a single dimension.

The 1-dimensional Fisher projections for each class pair are then modelled as two Gaussians (one for each class). For each class of projected 1-dimensional points, the mean μ and standard deviation σ are computed. The distribution for the set of points is assumed to be the univariate Gaussian function

$$g(x, \mu, \sigma) = \frac{1}{\sqrt{2\pi}\sigma} \exp\left[-0.5\left(\frac{x-\mu}{\sigma}\right)^2\right] \qquad (22)$$

Hence, for each pair there are 2 probability distributions. Given these 2 distributions, we use Bayesian decision theory to classify a feature. A pattern **x** is classified into class ω_i if

$$P(\omega_i \mid \mathbf{x}) = max(P(\omega_1 \mid \mathbf{x}), P(\omega_2 \mid \mathbf{x})) \qquad (23)$$

where $P(\omega \mid x)$ can be determined using Eq. (22) for a particular class. For the ten discriminants, there are ten outputs. The class label of a feature is defined as being the most common label in the ten outputs. In the case of a tie, a class is assigned randomly from those in the tie set. The final regions are renamed such that PUPIL, REFLECTION, SKIN and EYELASH are denoted NON-IRIS.

Iris segmentation using pattern classification: Once features are extracted from an image, they are either used as input to the training algorithm or the image segmentation algorithm. The method of segmentation that we use is region growing. Regions are grown by clustering the feature vectors, where each cluster represents an image region. Image regions are identified by classifying the cluster centroids using the Fisher linear discriminant. The clustering algorithm has parameters that need to be supplied and a stopping criterion to be defined. For simplicity and completeness, it is assumed that the stopping criterion for the iterative process is a binary function s that uses the change in centroids at the current iteration and the previous iteration to decide whether to proceed or not.
Let the centroids at step k be $C_k = \{\mathbf{c}_k^1, \mathbf{c}_k^2, \ldots, \mathbf{c}_k^n\}$ and let the centroids at step $k-1$ be $C_{k-1} = \{\mathbf{c}_{k-1}^1, \mathbf{c}_{k-1}^2, \ldots, \mathbf{c}_{k-1}^n\}$ where n is the number of centroids. Then

$$s(C_K, C_{K-1}) = \begin{cases} 0, \mid \mathbf{c}_k^i - \mathbf{c}_{k-1}^i \mid \leq \epsilon, \ \forall i = 1 \ldots n \\ 1, \text{otherwise} \end{cases} \qquad (24)$$

The clustering process runs as long as s evaluates to 1. A maximum number of iterations (80) is also introduced so that the process is not exhaustive. We use function s for the fuzzy clustering since evaluating a stopping criterion for the membership matrix U is computationally burdensome. The fuzzy factor m is 2 and $\epsilon = 0.0001$. The number of classes for the clustering algorithm is 6. More details regarding computing the number of clusters can be found in [11]. The Euclidean distance is used as a measure of pattern similarity.

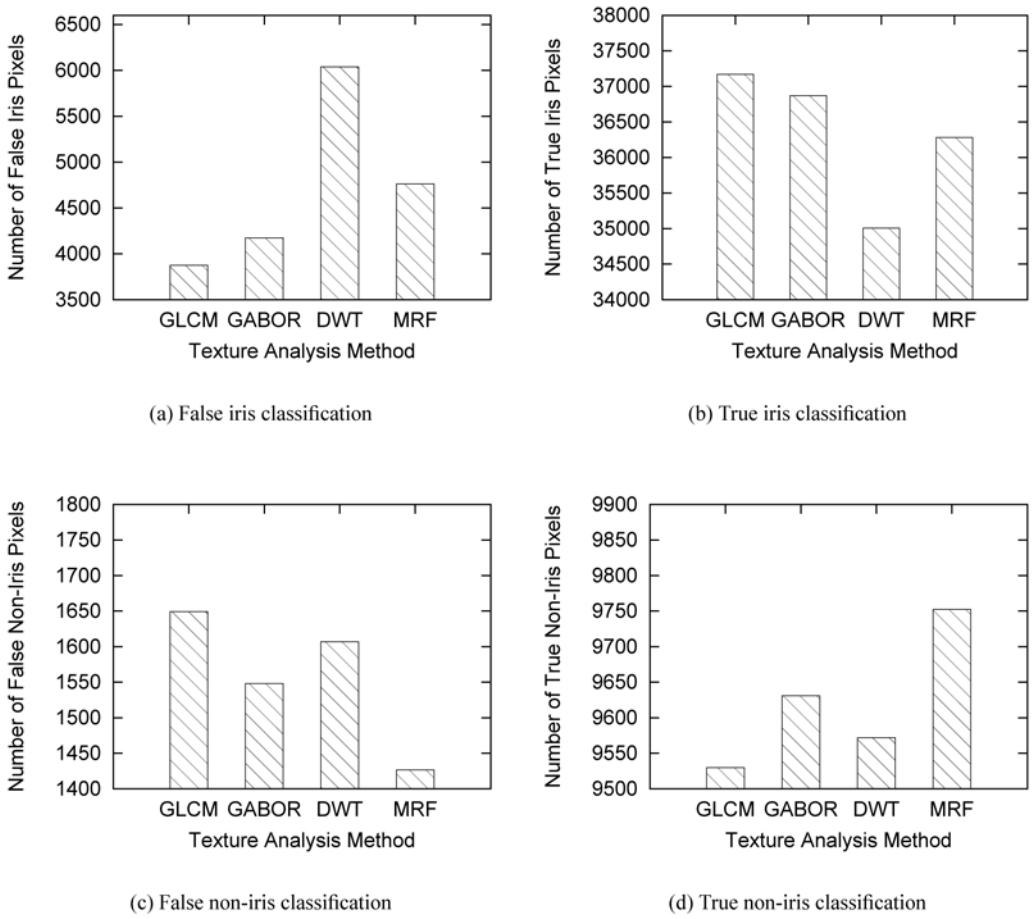

(a) False iris classification

(b) True iris classification

(c) False non-iris classification

(d) True non-iris classification

Figure 4: Test results

3. EXPERIMENTAL RESULTS AND DISCUSSION

100 test images were selected from the CASIA image database for experimental analysis. Ground truths for these input images were created manually by a human operator. The segmentation algorithm described in the previous section is executed 4 times, each time using one of the 4 texture descriptors, for each input image. Since the fuzzy clustering algorithm is randomly initialized, there is a possibility that it settles in a local optimum. Therefore, we perform 10 clustering test runs for each texture descriptor and then compute the average number of true and false pixel classifications for the 2 classes (IRIS and NON-IRIS) for each image; the number of pixels in an input iris image is 52224. The 100 segmentation results for each method are then averaged to produce the final outcome.

Figure 4 shows the results obtained. In order to evaluate the performance of each method, we considered the segmentation accuracy at the finest level i.e. pixels. This way, distinctions could easily be made since the segmentation accuracy viewed as a percentage for each class type does not appear significant across the different methods. We summarize the results:

- **IRIS:** GLCM performs the best for segmenting IRIS texture. On average, it segments 300 pixels more than the next best method (GABOR). The GABOR performs second best for this texture class. The MRF, segmenting 589 pixels less than GABOR, lies in third place. DWT performs the worst amongst the four methods for segmenting IRIS texture. On average, it segments 2163 pixels fewer than the GLCM.
- **NON-IRIS:** MRF provides the best discrimination for NON-IRIS pixels. However, as seen above, it performs poorly on IRIS pixels. The GABOR functions perform second best for this class of pixels (segments 121 pixels less than MRF). The DWT and GLCM rank third and fourth respectively for this class of pixels. The GLCM, while providing the best segmentation for IRIS pixels, provides the worst performance for the NON-IRIS class.

Table 2 provides a summary of Figure 4 by listing the segmentation accuracy as a percentage. From a global point of view, the four methods differ by 1-5% in their abilities to segment each class. While this doesn't appear significant, one must keep in mind that the NON-IRIS artifacts tend to be small in size compared to the rest of

Texture Method	False Non-iris (%)	False Iris (%)	True Non-iris (%)	True Iris (%)
GLCM	14.8	9.4	85.2	90.6
GABOR	13.8	10.2	86.1	89.8
DWT	14.4	14.7	85.6	85.3
MRF	12.8	11.6	87.2	88.4

Table 2: Summary of results

the image. The observations above put this into perspective by showing that these measurements fall in the region of a few to several hundred pixels. This is sufficient to rank the different methods for quality of segmentation. Another observation is that no single method provides the best discrimination for IRIS and NON-IRIS classes. This highlights the fact that a texture feature set is suitable for a particular *type* of texture and cannot be expected to perform equally well with another type.

In Figure 5(a) and Figure 5(b), a normalized iris image and its segmentation, using the GLCM texture descriptor, is presented. Small regions, falsely classified as NON-IRIS texture, can be seen in the result. A connected components algorithm can be used to improve the segmentation by removing these components in the image [7]. This is shown in Figure 5(c).

Several false classifications for a GABOR filter output are shown in Figure 6. This also occurs in some cases when applying the other techniques. Several explanations for this occurrence are possible: i) the window size for computing texture features is too small, ii) the texture features themselves are poor descriptors and iii) the Fisher linear discriminant cannot easily separate the 2 types of classes.

The segmentation algorithm classifies and labels the image pixels into one of two categories - iris or non-iris. Using these labels, the iris texture is extracted, as shown in Figure 7. This is the final segmentation of an iris image. Most of the artifacts in the image are removed. Although the segmentation is not 100% accurate, it is very effective. The eyelashes, eyelids, reflection and pupil pixels have been removed to a great extent. The feasibility of a feature extraction and pattern classification approach for segmenting iris images has been demonstrated.

(a) Input iris image

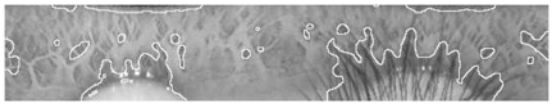

(b) Segmented image

(c) Connected components filtering

Figure 5: Segmentation result using GLCM texture features

(a) Input iris image

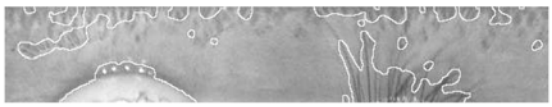

(b) Segmented image

Figure 6: Segmentation using GABOR features

4. CONCLUSIONS

In this paper, we focussed on the classic problem of image segmentation. Texture analysis and pattern recognition techniques are used to extract useful iris texture from an image of the eye. To our knowledge, this method of iris segmentation is new to the field and we have developed a feasible solution that provides good performance. The experimental results show that no single method tested in this paper can provide the best discrimination for the IRIS and NON-IRIS classes. The GABOR kernels provide good segmentation for both the IRIS and NON-IRIS classes; the GLCM method has the highest number of true classifications for IRIS pixels while the MRF performs

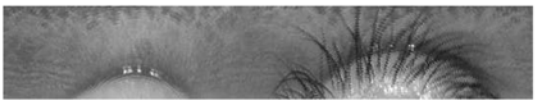

(a) Input iris image

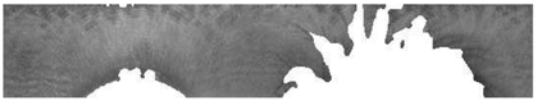

(b) Extracted iris texture

Figure 7: Extracted iris texture

similarly for NON-IRIS pixels. The DWT provides fair performance but it has the lowest accuracy amongst all the methods.

The feature sets used used in this study may not be ideal for iris texture description. Several other methods are present in the literature for further study e.g. Fourier descriptors, fractals and other wavelet functions. Optimal feature sets can be determined by using combinations of different features and assessing their segmentation or classification accuracy. Alternate techniques for constructing homogenous image regions, such as split-and-merge and the watershed algorithm, can also be found in the literature [7]. Many different pattern classification techniques are also available for study [38].

REFERENCES

[1] F. Adler, *Physiology of the eye*. St. Louis: MO:Mosby, 1965.

[2] W. Kong and D. Zhang, "Detecting eyelash and reflection for accurate iris segmentation," *International Journal of Pattern Recognition and Artificial Intelligence*, vol. 17, no. 6, pp. 1025–1034, 2003.

[3] J. Huang, Y. Wang, T. Tan, and J. Ciu, "A new iris segmentation method for recognition," in *International Conference on Image Processing*, vol. 3, 2004, pp. 554–557.

[4] L. Ma, T. Tan, Y. Wang and D. Zhang, "Personal identification based on iris texture analysis," *IEEE Trans. Pattern Analysis Mach. Intell.*, vol. 25, no. 12, pp. 1519–1533, 2003.

[5] "Casia Iris Database version 1." [Online]. Available: http://www.cbsr.ia.ac.cn/english/IrisDatabase.asp

[6] J. Canny, "A computational approach to edge detection," *IEEE Trans. Pattern Analysis and Mach. Intell.*, vol. 8, no. 6, pp. 679–698, Nov 1986.

[7] R. Gonzalez and R. Woods, *Digital Image Processing*. Addison-Wesley Publishing Company, 2002.

[8] M. A. Fischler and R. C. Bolles, "Random sample consensus: A paradigm for model fitting with applications to image analysis and automated cartography," *Comm. of the ACM*, vol. 24, pp. 381–395, 1981.

[9] J. Daugman, "High confidence visual recognition of persons by a test of statistical independance," *IEEE Trans. Pattern Analysis Mach. Intell.*, vol. 15, no. 11, pp. 1148–1961, 1993.

[10] E.H. Land, "Recent advances in retinex theory," *Vision Research*, vol. 26, no. 1, pp. 7–21, 1986.

[11] A. Bachoo, "Comparison of segmentation methods for an accurate iris extraction," Master of Science, School of Computer Science - University of KwaZulu-Natal, December 2006.

[12] B. Jähne, H. Haußecker and P. Geißler, *Handbook of Computer Vision and Applications - Volume 2*. Academic Press, 1999.

[13] M. Sonka, V. Hlavac and R. Boyle, *Image Processing: Analysis and Machine Vison*. PWS Publishing Company, 1999.

[14] A. Rosenfeld and A. Kak, *Digital picture processing*. Academic Press, 1982, vol. 1.

[15] A.K. Jain, *Fundamentals of digital image processing*. New Jersey: Prentice-Hall, 1989.

[16] C.H. Chen, L.F. Pau and P.S.P. Wang, *The Handbook of Pattern Recognition and Computer Vision (2nd Edition)*. World Scientific Publishing Co., 1998.

[17] R. Haralick, "Statistical and structural approaches to texture," *Proceedings of the IEEE*, vol. 67, no. 5, pp. 786–804, 1979.

[18] R.M. Haralick, K. Shanmugam and I. Dinstein, "Texture features for image classification," *IEEE Trans. System Man. Cybernat.*, vol. 8, no. 6, pp. 610–621, 1973.

[19] J.S. Weszka and A. Rosenfeld, "An application of texture analysis to material inspection," *Pattern Recognition*, vol. 8, pp. 195–199, 1976.

[20] L.S. Davies, S.A. Johns and J.K. Aggarwal, "Texture analysis using generalized co-occurence matrices," *IEEE Trans. on Patt. Anal. and Mach. Intell.*, vol. 1, no. 3, pp. 251–259, 1979.

[21] M.M. Trivedi, R.M. Haralick, R.W. Conners and S. Goh, "Object detection based on grey level co-occurrence," *Computer Vision, Graphics and Image Processing*, vol. 28, pp. 199–219, 1984.

[22] R.W. Conners and C.A. Harlow, "A theoretical comparison of texture algorithms," *IEEE Trans. on Patt. Anal. and Mach. Intell.*, vol. PAMI-2, pp. 204–222, 1980.

[23] Q. Zhang, J. Wang, P. Gong and P. Shi, "Study of urban spatial patterns from spot panchromatic imagery using textural analysis," *Int. J. Remote Sensing*, vol. 24, no. 21, pp. 4137–4160, 2003.

[24] S. Mallat, "A theory of multiresolution signal decomposition," *IEEE Trans. on Pattern Analysis and Machine Inteligence*, vol. 11, no. 7, pp. 674–693, 1989.

[25] M. Kokare and B. Biswas, "Texture image retrieval using rotated wavelet filters," *Pattern Recognition Letters*, no. 28, pp. 1240–1249, 2007.

[26] C.-W. Liang and p.-Y. Chen, "DWT based text localization," *International Journal of Applied Science and Engineering*, vol. 2, no. 1, pp. 105–116, 2004.

[27] J.-L. Starck, F. Murtagh and A. Bijaoui, *Image Processing and Data Analysis: The Multiscale Approach*. Cambridge University Press, 1998.

[28] D. Clausi, "Comparison and fusion of co-occurrence, Gabor and MRF texture features for classification of SAR sea-ice imagery," *Atmosphere-Ocean*, vol. 39, no. 3, pp. 183–194, 2001.

[29] B. Manjunath and W. Ma, "Texture features for browsing and retrieval of image data," *IEEE Trans. on Pattern Analysis and Machine Intelligence*, vol. 18, no. 8, pp. 837–842, 1996.

[30] S. Grigorescu, N. Petkov, and P. Kruizinga, "Comparison of texture features based on Gabor filters," *IEEE Trans. on Image Processing*, vol. 11, no. 10, pp. 1160–1167, 2002.

[31] P. Kruizinga and N. Petkov, "Nonlinear operator for orientated texture," *IEEE*, vol. 8, no. 10, pp. 1395–1407, 1999.

[32] A.K. Jain, N.K. Ratha and S. Lakshmanan, "Object detection using Gabor filters," *Pattern Recognition*, vol. 30, no. 2, pp. 295–309, 1997.

[33] D.A. Clausi and M.E. Jernigan, "Designing Gabor filters for optimal texture separability," *Pattern Recognition*, vol. 33, pp. 1835–1849, 2000.

[34] J. Woods, "Two-dimensional discrete Markovian fields," *IEEE Trans. Info. Theory*, vol. 18, no. 2, pp. 232–240, 1972.

[35] E. Cesmeli and D. Wang, "Texture segmentation using Gaussian-Markov random fields and neural oscillator networks," *IEEE Trans. on Neural Networks*, vol. 12, no. 2, pp. 394–404, 2001.

[36] J. Dunn, "A fuzzy relative of the isodata process and its use in detecting compact well separated clusters," *Journal of Cybernetics*, vol. 3, pp. 32–57, 1974.

[37] J. Bezdek, *Pattern Recognition with Fuzzy Object Function*. Plenum Press, 1981.

[38] R.O. Duda, P.E. Hart and D.G. Stork, *Pattern classification*. John Wiley and Sons, 2001.

OPTIMAL ALLOCATION OF FACTS DEVICES: CLASSICAL VERSUS METAHEURISTC APPROACHES

Y. Del Valle*, J. Perkel*, G. K. Venayagamoorthy**, and R. G. Harley*

* *Department of Electrical and Computer Engineering, Georgia Institute of Technology, Atlanta, GA 30332 USA. Email: yamille.delvalle@gatech.edu*

** *Real-Time Power and Intelligent Systems Laboratory, Department of Electrical and Computer Engineering, Missouri University of Science and Technology, Rolla, MO 65409 USA*

Abstract: The application of optimization techniques to allocate and size FACTS devices in a power system is still under study. Currently, there is no widely accepted method since many researchers claim their methods to be better than others. This paper compares the effectiveness of classical and metaheuristic optimization approaches in a simple but realistic case study of optimal allocation of FACTS (Flexible AC Transmission System) devices, considering steady state and economic criteria. Concepts and details about the optimization process that tend to be overlooked in the literature are discussed together with some considerations about statistical analyses in the case of metaheuristic approaches.

Keywords: FACTS devices, classical optimization, Benders' decomposition, branch and bound, evolutionary computation techniques, genetic algorithm, particle swarm optimization, bacterial foraging algorithm.

1. INTRODUCTION

The topic of optimal allocation of FACTS (Flexible AC Transmission System) devices is still in a relatively early stage of investigation. Currently, there is no widely accepted method in the academic circles since many researchers claim their methods to be "better" than others. Considering the present state-of-the-art in this area, the comparison of different methods, particularly between classical and metaheuristic approaches, has been difficult to evaluate because each study focuses on different problem formulations, system sizes and conditions.

This paper provides a common background for comparing the performance of classical and metaheuristic optimization algorithms. A simple but realistic case study of optimal STATCOM allocation (a type of FACTS devices), considering steady state and economic criteria, is used to assess the performance of two classical methods: Bender's decomposition and Branch-and-Bound (B&B), and four metaheuristic approaches: Genetic Algorithm (GA), Particle Swarm Optimization (PSO), Enhanced-PSO, and Bacterial Foraging Algorithm (BFA).

It is important to note that the focus of this paper is not to find a solution to the particular problem, but rather to illustrate and comment on important details about the optimization process that tend to be overlooked in the literature and are unknown to most readers: the discussion about local versus global optimality (for a given objective function), understanding convexity assumptions (that do not apply only to the objective function), and the importance of the algorithm's convergence into feasible regions. Moreover, considering metaheuristic approaches, a statistical analysis is required to evaluate their performance since the use of the typical average and standard deviations must be validated to be meaningful.

The following sections of this paper provide: an optimization background (section 2), concepts and issues that should not be disregarded (section 3), a problem description (section 4), optimization algorithms (section 5), simulation results (section 6), and concluding remarks (section 7).

2. BACKGROUND

The optimization techniques used to solve the optimal allocation of FACTS devices can be decomposed into two primary groups: classical approaches and metaheuristic algorithms, consisting of mainly evolutionary computation techniques (ECTs). A third group of alternative methods, such as modal analysis, may also be considered. However, these methods are primarily based on technical feasibility rather than on finding optimal solutions.

2.1 Classical Optimization Techniques

In the literature, two classes of classical optimization methodologies have been applied to this problem: (i) Mixed Integer Linear Programming (MILP) [1]-[3] and (ii) Mixed Integer Non-Linear Programming (MINLP) [4]-[6].

The MILP formulation, as the name indicates, requires the relationships between all variables to be linear. Thus, this approach can be only used together with DC power flow. The main algorithms for solving the MILP problem are Bender's Decomposition [1], Branch and Bound (B&B), and Gomory cuts [2], [3]. The concluding remarks of the MILP approach indicate that the optimization process is performed in an efficient manner, but the DC power flow represents a limitation for the type problems that can be addressed.

The MINLP formulation allows for the use of non-linear objective function and constraints, thus, AC power flow can be used in this case. The algorithm most widely utilized for solving the MINLP problem is Bender's Decomposition [4]-[6]. Unfortunately, it has been reported that the size and non-convexity of the problem, which depend on the system parameters, are critical issues that may cause convergence problems.

2.2 Metaheuristic Techniques

Computational intelligence based techniques, such as Genetic Algorithm (GA) [4], [5], [7]-[10], Particle Swarm Optimization (PSO) [11]-[13], Simulated Annealing (SA) [7], [14], Tabu Search (TS) [13], [14], and Evolutionary Programming (EP) [15], [16], are alternative methods for solving complex optimization problems.

Candidate solutions play the role of individuals in a population and the cost function determines the environment where the solutions exist. Evolution of the population then takes place and, after the repeated application of biological or social operators, the optimal solution is reached. In general ECTs perform well in MINLP problems. However the scalability of these methods requires further investigation.

3. OPTIMIZATION: CONCEPTS AND ISSUES

3.1 Optimization of offline problems

A common misperception is the belief that the problem of optimal allocation of FACTS devices is not challenging from the optimization perspective because it is an offline problem. Some presume that the solution is as simple as arranging a number of computers in parallel and letting them run, for as long as it takes, until all possible solutions are found and the best one selected among them.

The fact is that, even when this approach is theoretically possible to perform for any system, in practice the number of calculations required to find the solutions to the problem can grow extremely fast as the size of the system increases and the objective function becomes more sophisticated (evaluation of transient performance is computationally intensive). If it is also required to satisfy the N-1 or N-2 contingency criteria, or add stochastic components and uncertainties to the system, the number of cases to evaluate simply becomes uncountable.

Therefore, the study of optimization algorithms applied to system planning problems, such as the problem of FACTS allocation is not trivial.

3.2 Convexity assumptions

The concept of convexity is mostly analyzed in the case of the objective function: if the function is strictly convex a unique optimal solution is guaranteed (Fig. 1.a).

This characteristic is most desirable but it rarely occurs in power system problems. Most of the time the plot of the objective function resembles the function in Fig. 1.b. As a result, gradient descent algorithms are prone to getting trapped in local valleys (local minima). In these cases, special mechanisms, such as injecting randomness to the search, must be considered.

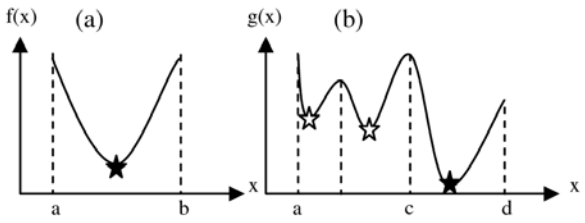

Fig. 1: Global versus local minima

The convexity assumption also applies to the feasible region. For example, in the case of linear programming problems, the optimum can be found (either by simplex method or interior point method) if the feasible region is a convex set, as shown in Fig. 2.a (as opposed to Fig, 2.b) [17].

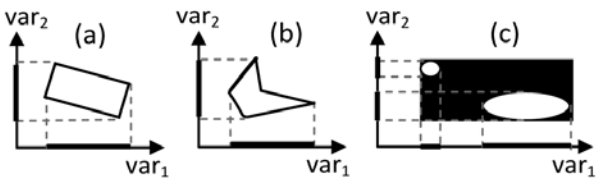

Fig. 2: Convexity of the feasible region

A worst case is presented in Fig. 2.c. where the feasible region consists of several small areas (white) scattered among the area limited by the upper and lower bounds of the decision variables, var_1 and var_2 (black area).

This type of feasible region, as shown later in the paper, is typical when technical constraints are imposed in the power system. The optimization algorithms in this case should have efficient exploration mechanisms so that feasible solutions can be found fast and therefore minimum computational effort is wasted wandering around in infeasible areas.

3.3 Global Optimality

Another aspect that tends to be overlooked in the literature is the discussion of global versus local optimality. Contrary to general opinion, this topic is not related to comparing the values of different objective functions applied to the same power system. Instead, it implies the understanding that, for a given objective function, the problem may a have a unique optimal solution, thus a local optimum is also the global optimum (Fig. 1.a) or the problem may have several local optimal points plus the global optimum. Fig. 1.b represents the latter, where the first white star represent the minimum in the interval [a, b], the second white star is the local minimum in the interval [b, c], and the black star is global minimum in the overall interval [a, d].

The previous concept may seem superfluous, however once an optimization algorithm provides a solution, normally there are no guarantees about its quality. Proof of global optimality can be obtained but only under very specific conditions as in the case of linear programming problems [17]. In the case of MINLP problems, the capability of each algorithm to find the global optimum, without getting trapped in local minima, has to be studied separately.

3.4 Statistical Analysis for metaheuristic methods

Particularly, in the case of metaheuristic algorithms, statistical analysis is required to assess their performance. It is important to note that, currently in literature, the main statistical values used to compare the performance among different metaheuristic optimization algorithms are the mean value of the objective function and its standard deviation.

Intuitively, most people, with some statistical background, understand the average value as the expected outcome of a specific trial and the standard deviation as a measure of the variability of this outcome, nevertheless this true meaning can be concluded if and only if the data comes from a Gaussian distribution.

In the literature, results for a normality test, such as the Anderson-Darling, the Shapiro-Wilk or similar tests, are not typically reported, therefore conclusions about the performance of the optimization methods may be questionable. An example when the data do not distribute normal will be shown to illustrate the importance of this issue. In that case, other statistical tools like Weibull analysis must be used to derive conclusions that are statistically significant.

4. PROBLEM DESCRIPTION

The problem to be addressed consists of finding the optimal placement (bus number) and power rating (MVA) of multiple STATCOM units in a 45 bus system, part of the Brazilian power network (Fig. 3) [18].

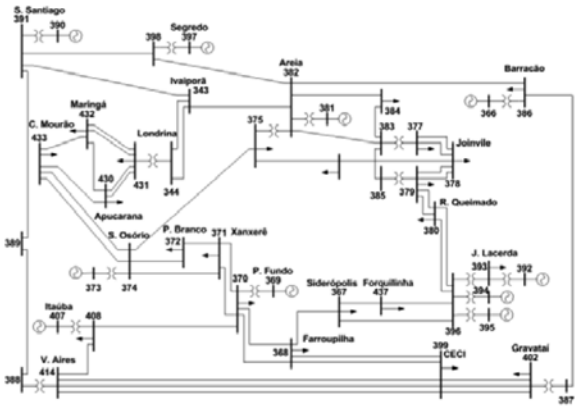

Fig. 3: 45 Bus section of the Brazilian power system

The main objective is to minimize the bus voltage deviations throughout the power system at minimum cost. The reasons for selecting the objective criteria and specific power system are: (i) the power system is not large; therefore an exhaustive manual search can be performed to find the global optimum, (ii) the problem has a reduced, scattered and non convex feasible region, and (iii) only a steady state criterion is considered to avoid possible discrepancies when transient analysis is also included [19].

4.1 Objective Function

Two goals are considered: (i) to minimize voltage deviations in the system and (ii) to minimize the cost. Thus, two metrics J_1 and J_2 are defined as in (1) and (3).

$$J_1 = \sqrt{\sum_{1}^{N} (V_k - 1)^2} \tag{1}$$

Where:

J_1 is the voltage deviation metric,
V_k is the p.u. value of the voltage at bus k, and
N is the total number of buses.

The total cost function, C_{total}, consists of two components: a fixed cost per unit that is installed in the system and a variable cost that is a linear function of each unit size:

$$C_{total}(M) = C_f \cdot M + C_v \cdot \sum_{p=1}^{M} \eta_p \quad (2)$$

Where:

M is the number of units to be allocated,
C_f is the fixed cost per unit,
C_v is the cost per MVA, and
η_p is the size in MVA of unit p.

Since $C_f >> C_v$, it is convenient to normalize each term of the cost function prior to its inclusion in the objective function (3).

$$J_2 = \frac{C_f \cdot M}{C_f \cdot M_{\max}} + \frac{C_v \cdot \sum_{p=1}^{M} \eta_p}{C_v \cdot M_{\max} \cdot \eta_{\max}} = \frac{M}{M_{\max}} + \frac{\sum_{p=1}^{M} \eta_p}{Max\_MVA} \quad (3)$$

Where:

J_2 is the cost metric,
M_{max} is the maximum number of STATCOM units to be allocated, and
η_{max} is the maximum size in MVA of each STATCOM unit.

The multi-objective optimization problem can now be defined using the weighted sum of both metrics J_1 and J_2 to create the overall objective function J shown in (4).

$$J = \omega_1 \cdot J_1 + \omega_2 \cdot J_2 \quad (4)$$

The weight for each metric is adjusted to reflect the relative importance of each goal. In this case, considering the maximum magnitudes of J_1 and J_2, it is decided to assign values of $\omega_1 = 1$ and $\omega_2 = 0.5$, such that both metrics have equal importance.

4.2 Decision Variables

The decision variables are the location of the STATCOM units and their sizes. These variables can be arranged in a vector as:

$$x_i = [\lambda_1 \quad \eta_1 \quad \ldots \quad \lambda_M \quad \eta_M] \quad (5)$$

Where:

λ_p, $p=1...M$, is the location (bus number) of STATCOM unit p.

All components of the decision vector are integer numbers, thus $x_i \in Z^{2M}$.

4.3 Constraints

There are several constraints in this problem regarding the characteristics of the power system and the desired voltage profile. Each constraint represents a limit in the search space, which in this particular case corresponds to:

-
  Generator buses are omitted from the search process since they have voltage regulators to regulate the voltage.
- Bus numbers are limited to {1, 2,…, *N*}.
- Only one unit can be connected at each bus.
- The number of units: 1 M 5.
- The size of each unit: 0 η_p 250 MVA.
- The desired voltage profile requires N additional restrictions defined as:

$$0.95 \le V_k \le 1.05 , \quad \forall k \in \{1,2,...,N\} \quad (6)$$

Each solution that does not satisfy the above constraints is considered infeasible.

5. OPTIMIZATION ALGORITHMS

For the optimal allocation of multiple FACTS units in a 45 bus system, six algorithms are fully developed and compared: Bender's decomposition, B&B, GA, PSO, Enhanced-PSO, and BFA.

5.1 Benders' Decomposition

This method separates two sets of decisions that are made into two consecutive stages. In the first stage of the decision making, some of the constraints are delayed to reduce the complexity of the original (master) problem. In the second stage, some of the parameters that influence the decision, whose values were originally uncertain, are known and fixed after the first decision vector is found. Thus the secondary problem is reduced in complexity and in the number of variables [20], [21].

In the case of the STATCOM allocation problem, the master problem considers the decision vector in (5) that

can be naturally separated into one sub-vector for selecting optimal locations and another sub-vector for choosing optimal sizes.

The separation of the constraints can be stated as follows:

- First stage: sizes of the STATCOM units become delayed constraints, thus the reactive power limits for these devices are relaxed in the solution of the power flow. The voltage reference is set to 1.0 p.u. for each STATCOM controller. The objective function corresponds to the voltage deviation metric defined in (1).

- Second stage: with the locations of the devices determined, the set of constraints is limited to those related with the maximum size of each unit. The objective function includes the voltage deviation metric and the cost metric as in (4).

5.2 Branch and Bound

B&B is a classical approach to search for an optimal solution by evaluating only a subset of the total possible solutions. The main steps in the algorithm are [17], [20], [21]:

- Branching: the set of feasible solutions is partitioned into simpler subsets. At each iteration, one of the promising subsets is chosen and an effort is made to find the best feasible solution within it.
- Bounding: the algorithm proceeds to find upper and lower bounds for the optimal objective value. There is only one upper bound u at each stage, which corresponds to the lowest among the objective values of all the feasible solutions that have appeared so far.
- Pruning: if at certain a stage, one of the subsets has a lower bound which is greater than the current upper bound, then the algorithm prunes (discards) that set.

Branching, bounding and pruning are repeated until the optimal solution is found.

For this particular problem, the objective function is defined as in (4). The branching strategy corresponds to the "depth-first search": for each subset of feasible locations, branching is performed by dividing progressively the STATCOM size intervals into smaller sub-intervals. The bounding and pruning strategies help to narrow the search by discarding as many sub-intervals as possible until the optimal value, for the particular subset of feasible locations, is found. In the next stage another subset of feasible locations is chosen, and the process is repeated until the set of all feasible locations is covered.

5.3 Genetic Algorithm (GA)

GA is an ECT that patterns itself after Charles Darwin's "survival of the fittest" concept. Each chromosome represents a possible solution to the problem. Through selection of parents, crossover between members of the current population, and mutation of the offspring, the population evolves and, after a number of generations, it approaches an optimal solution [22], [23].

For this particular problem, the chromosomes are defined as the decision vector in (5) and the fitness of each chromosome is evaluated through the use of the objective function in (4).

After the fitness of the entire population has been assessed, a subgroup of chromosomes is selected to become the parents for the next generation. For this particular case, elitism and "roulette wheel" are used as the selection mechanisms. Once the two parents are chosen, crossover between them produces two offspring. For each offspring, there is a chance that any number of its genes may be mutated; the mutation probability applies to each gene independently resulting in anywhere from zero to all genes being mutated.

The previous generation is replaced by the new generation and the entire process is repeated until the maximum number of generations is reached.

The parameters used in this study are shown in Table I [24].

Table 1: GA Parameters

Parameter	Optimal value
Percentage of elite members	10%
Crossover probability	85%
Mutation probability	5%

5.4 Particle Swarm Optimization (PSO)

The PSO algorithm considers that each particle represents a potential solution to the problem, thus the particles are defined as the decision vector in (5). The quality of the solution, that allows the best position for each particle and the swarm to be determined, is assessed using the fitness function defined in (4).

At each iteration, t, the position of each particle is determined by [25], [26]:

$$\vec{x}_i(t) = \vec{x}_i(t-1) + \vec{v}_i(t) \tag{7}$$

The velocity of each particle is determined by both the individual and group experiences:

$$\begin{aligned} v_i(t) = {} & w_i \cdot v_i(t-1) + \ldots \\ & c_1 \cdot r_1 \cdot (p_i - x_i(t-1)) + \ldots \\ & c_2 \cdot r_2 \cdot (p_g - x_i(t-1)) \end{aligned} \tag{8}$$

Where:

w_1 is a positive number between 0 and 1,
c_1 and c_2 are the cognitive and social acceleration constants respectively,
r_1 and r_2 are random numbers with uniform distribution in the range of [0, 1].
p_i is the individual best position found by the corresponding particle, and
p_g is the global best position found by the entire swarm.

To avoid the divergence of the swarm, a maximum velocity for each dimension of the problem hyperspace is defined (v_{max}).

Additionally, since integer variables are included in the optimization problem, the Integer-PSO version is used, where the particle's position is rounded off to the nearest integer [26].

The PSO parameters used in this study are presented in Table II [24].

Table 2: PSO Parameters

Parameter	Optimal value
Inertia constant (w_i)	Linear decrease (0.9 to 0.1)
Individual acceleration constant (c_1)	2.5
Social acceleration constant (c_2)	1.5
V_{max} for bus location	9
V_{max} for STATCOM size	50

5.5 Enhanced-PSO

For this particular application, the canonical PSO algorithm described in the previous section is enhanced to facilitate the search through the problem hyperspace [24].

The additional logic in each individual is defined by the following rules:

- If the corresponding particle's best position, *pbest,* and the swarm's best position, *gbest,* are both feasible solutions then the velocity update is performed according to (8).
- If the particle has not found a feasible solution yet, then it is better to rely on the social knowledge and the velocity update equation is replaced by:

$$v_i(t) = w_i \cdot v_i(t-1) + c \cdot rand \cdot (p_g - x_i(t-1)) \qquad (9)$$

Where:
c is a single acceleration constant: $c = c_1 + c_2$,
rand is a random number with uniform distribution in the range of [0, 1].

- If none of the particles have found a feasible solution (*gbest* and *pbest* values are both infeasible)

then the velocity of each particle is updated using a random value of the maximum velocity as shown in (10).

$$v_i(t) = \left[r_1 \cdot v_{\max}(1) \quad r_2 \cdot v_{\max}(2) \quad r_3 \cdot v_{\max}(3) \quad r_4 \cdot v_{\max}(4)\right] \qquad (10)$$

Where:
r_h is a random number with uniform distribution in the range of [0, 1] and
$v_{max}(h)$ is the maximum velocity in the h^{th} dimension of the problem hyperspace.

5.6 Bacterial Foraging Algorithm (BFA)

BFA is based on the movement patterns of *E. coli* in the intestines. Each individual, in this case a bacterium, represents a possible solution to the problem as in (5).

The algorithm considers four successive steps [26], [28]:

- Chemotaxis: the bacteria move towards better nutrient concentrations. For the N_c chemotactic steps the direction of movement is given by:

$$\theta^i(j+1,k,l) = \theta(j,k,l) + C(i) \cdot \varphi(j) \qquad (11)$$

Where :
$C(i)$ is the step size,
j is the number of chemotactic step, k is the reproduction step, and l is the index for the elimination event.
$\varphi(j)$ is the unit length of random direction taken at each step.

The bacterium continues to move in the same direction (given that the fitness function value improves) and stops when the number of repetitions reaches a maximum of N_s.

- Swarming: All the bacteria have a cell-to-cell attraction via attractant and a cell-to-cell repulsion via repellant, with respect to other bacteria. Thus the movement of each bacterium towards better nutrient concentrations can be represented by:

$$J_o(i,j,k,l) + J_{cc}(\theta, P) \qquad (12)$$

Where:
$J_o(i,j,k,l)$ is the fitness function and
J_{cc} is the term that defines the attraction-repulsion to other bacteria [24].

The fitness function, J_o, corresponds to the objective function in (4) plus a penalty function defined as the number of buses in the system that violate the voltage profile constraint in (6).

- Reproduction: after chemotaxis, the population of bacteria is allowed to reproduce. S_r (S_r=$S/2$) bacteria having the worst objective function value die and the remaining part split into two keeping the population size constant.

- Elimination-Dispersal: each bacterium is eliminated with a probability of p_{ed}.

The BFA parameters used in this study are [24]:

Table 3: BFA Parameters

Parameter	Optimal value
Number of bacteria (S)	20
Number of chemotactic cycles (N_c)	30
Number of swim steps (N_s)	3
Number of reproductions (N_{re})	3
Number of elimination-dispersal loops (N_{ed})	2
Probability of elimination (P_{ed})	0.5
Maximum distance ($C(i)$)	4
Attraction coefficients $d_{attract}$ and $w_{attract}$	0.1
Repellent coefficient d_{repel} and w_{repel}	0.05

6. SIMULATION RESULTS

6.1 Exhaustive search

An exhaustive search is performed on the problem of optimally allocating M STATCOMS to the power system in Fig. 3 by running a powerflow solution for each case in order to determine the global optimum. The solution indicates that the minimum number of devices needed to satisfy the constraints in Section IV-C is two and the computational effort corresponds to 37,196,250 power flows.

The feasible region of the problem is reduced, scattered and non convex. It is not possible to plot the entire feasible region since the dimensions are greater than three, however for illustrative purposes Fig. 4 shows the best scenario considering all possible bus locations and maximum STATCOM size of 250 MVA for each unit.

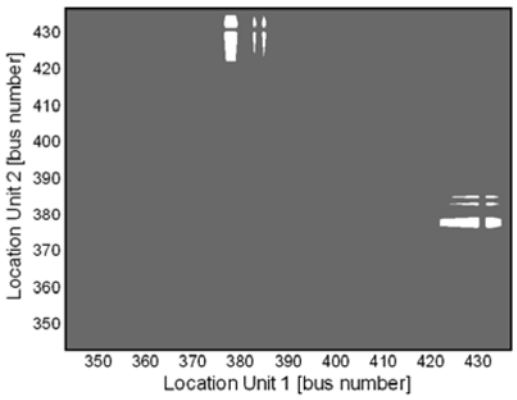

Fig. 4: Feasible region (white) vs. problem hyperspace

Fig. 5 shows the percentage of the feasible region with respect to the total number of cases [24].

Fig. 5 (a): Percentage of feasible locations over total possible combinations. (b): Percentage of feasible solutions over total problem hyperspace

The global optimal solution is to place one STATCOM unit of 75 MVA at bus 378 and the second unit of 92 MVA at bus 433. The effect of the two STATCOM units is shown in Fig.6.

After the devices are optimally placed, all bus voltages are in the desired range of ±5% voltage deviation. Additionally, the voltage deviation metric J_1 improves by 26.5 % from an original value of 0.2482 to 0.1824.

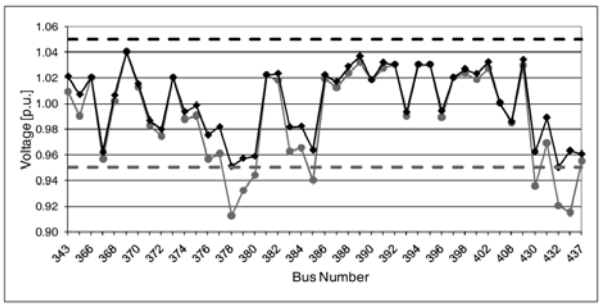

Fig. 6: Voltage profile without (-•-) and with STATCOM units (-♦-)

6.2 Metaheuristic approaches

Convergence into feasible regions: In order to evaluate the performance of the metaheuristic optimization algorithms (GA, PSO, Enhanced-PSO, and BFA), 150 trials are carried out for each algorithm. At each trial, the number of power flow evaluations (PF) is recorded until the first feasible solution is found. If no feasible solution is found, then the algorithm stops when the number of power flow evaluations reaches a maximum of 2000 [24]. Additionally, a performance indicator called Success Rate is calculated to determine the percentage of time that the algorithm is able to converge into feasible regions.

The Anderson-Darling normality test is performed to determine if the datasets for each algorithm are normally distributed. The results of this analysis show that with better than 99.5% certainty, the data are not normally distributed. Thus, other statistical distributions must be used.

The Weibull distribution is an appropriate alternative to analyze data of this type. This distribution is used extensively to study extreme-value data. In this case, the number of power flows to the *first* feasible solution [29] corresponds to such extreme-value data.

A two-parameter Weibull distribution is fitted to each dataset in the least-squares sense. In each case, the correlation is greater than 0.95, indicating that the choice of Weibull is suitable. Fig. 7 shows the resulting probability plots for each technique and Table IV shows the corresponding statistical parameters.

Table 4: Statistical values two-parameter Weibull Distribution

	GA	PSO	Enhanced PSO	BFA
Minimum PF	67	28	22	24
Maximum PF	>2000	>2000	379	1834
Success Rate	30	20.7	100	100
Scale (α)	4329	8650	147	326
Shape (β)	1.1	0.8	2.5	1.2

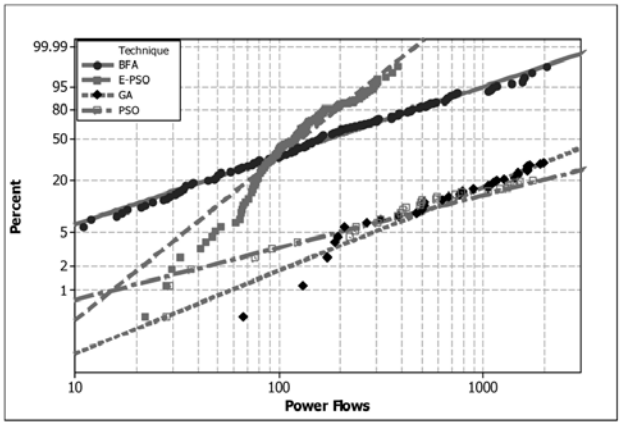

Fig. 7: Weibull plots of all algorithms

Table IV indicates that, based on the ranges for the number of power flow evaluations, the Enhanced-PSO is faster in finding feasible solutions compared to the other algorithms. Moreover its Success Rate is 100% versus 20.7% for canonical PSO and 30% in the case of GA.

Additionally, the Weibull parameters, α and β, carry important physical meanings. The scale parameter, α, corresponds to the characteristic time to find the first feasible solution. This is defined as the number of power flows needed to obtain a feasible solution in 63.2% of the trials. The shape parameter, β, represents the slope produced by data when plotted on a Weibull plot (Fig. 7). More interestingly, the shape parameter provides insight into how the algorithms are able to seek out feasible solutions:

- $\beta < 1$: Less likely to find feasible solutions as the number of power flows increases.
- $\beta = 1$: Same likelihood of finding feasible solution regardless of the number of power flows that are performed.
- $\beta > 1$: As the number of power flows increases so does the likelihood of locating a feasible solution.

Applying these concepts, the resulting characteristic time to find a feasible solution is 147 and 326 power flows for Enhanced-PSO and BFA, respectively. The canonical PSO and GA are only able to find feasible solutions in at most 30% of the trials while the rest of the values are censored. This leads to characteristic times of 4329 and 8650 for GA and PSO, respectively.

In addition, the Enhanced-PSO is the only algorithm with a shape parameter grater than one, which means that this algorithm offers the most efficient means of locating feasible regions.

The probability of obtaining a feasible solution in any number of power flows (or less) for each of the techniques, can also be read off from Fig. 7. Equally, the probability may be specified and then the maximum number of power flows required to find feasible regions may be read off.

Global Optimality: For further comparison of the performance of Enhanced-PSO and BFA algorithms, their capabilities for finding the global optimal solution are investigated. Thus, statistical values are calculated over a set of 50 trials, with 20 particles and 100 iterations, for each algorithm. In this case, the Anderson-Darling normality test gives *p*-values greater than 0.05, indicating that the data have a Normal distribution for both cases. Table V provides the additional indicators to evaluate the accuracy in finding the optimal solutions.

TABLE 5: Statistical analysis for optimal solutions

Parameter	Enhanced PSO	BFA
Minimum *J* value	0.91745	0.92441
Maximum *J* value	1.08390	1.36422
Average *J* value	0.98791	1.14765
Standard deviation *J* value	0.04167	0.09654

The accuracy in finding the optimal solution is higher in the case of the Enhanced-PSO algorithm with a standard deviation of 0.0417 as compared to 0.0965 of BFA, which is more than two times larger. In terms of the maximum and average values of the objective function value, they indicate a clear advantage of the Enhanced-PSO over BFA. Furthermore, the Enhanced-PSO algorithm finds the global optimum for this problem.

Figure 8 shows the degree of sub-optimality in the solutions provided by the Enhanced–PSO algorithm. It is possible to note that 70% of the time, the solutions found have 10% or less difference with respect to the global optimum. Additionally, the difference does not exceed the value of 20% in any of the trials.

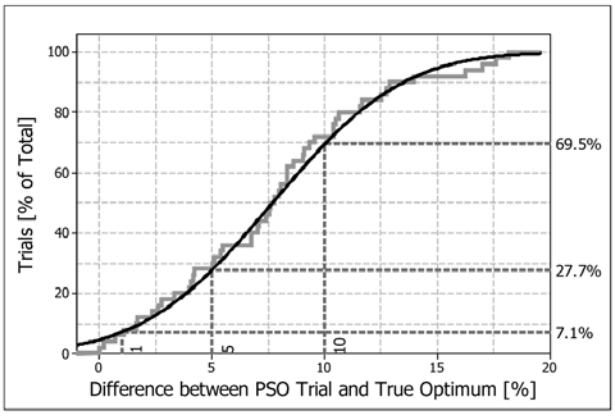

Fig. 8: Degree of sub-optimality for Enhanced-PSO algorithm

Scalability: As the previous section demonstrates, the evolutionary computation techniques are able to find solutions in a small fraction of the number of power flows required for an exhaustive search. One aspect of concern about their use is their capability to effectively solve optimization problems when the size of the power system is increased.

The Enhanced-PSO algorithm is applied to illustrate how the algorithm performs when the power system is changed from the Brazilian 45 bus system to the IEEE 118 bus network [30].

Figure 9 shows the capability of the algorithm to converge into feasible regions using boxplots (the box represents the middle 50% of data). The maximum number of iterations is 100 for both cases and the number of particles are 20 and 50 for the 45 bus and 118 bus system respectively. This figure provides evidence that the performance of the algorithm is not substantially affected by the size of the system. In both cases, feasible solutions are found in fewer than 17% of the maximum allowed power flow computations and the inter-quartile ranges (difference between the first and third quartile, that spans the middle 50% of the data) are fairly similar (4.5% and 5% for 45 bus and 118 bus systems respectively).

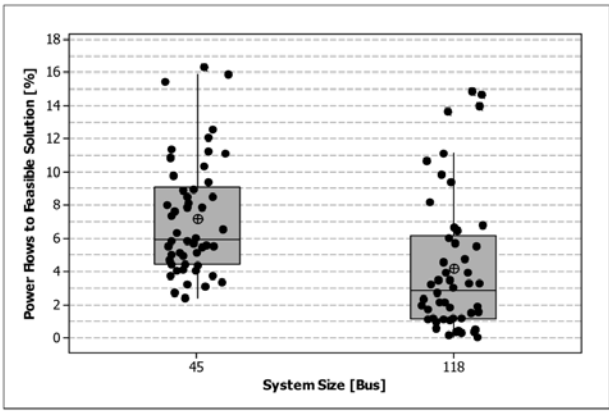

Fig. 9: Convergence into feasible regions

Due to the large number of power flow computations, an exhaustive search is not performed for this case. To give an idea of the computational time involved, for one power flow computation taking 125 msec, then the total time to run exhaustive search in the 45 bus system is 54 days, however for the 118 bus system the total time is 475 days (almost one year and four months). For this reason, the quality of the optimal solutions is assessed only by statistical analysis over 50 trials.

Table VI, shows the results for the 45 bus and 118 bus systems. The maximum, average and standard deviation values are presented as percentages with respect to the minimum objective function value.

Table 6: Optimal solutions – 45 and118 bus system

Parameter	45 Bus	118 Bus
Minimum *J* value	0.91745	0.8734
Maximum *J* value [%]	118.1	109.2
Average *J* value [%]	107.7	100.7
Standard deviation [%]	4.54	1.34

Comparing the percentages in both columns, it is possible to conclude that there are not significant differences in the performance when the size of the power system is increased.

6.3 Classical versus metaheuristic approaches

Table VII summarizes the overall performance data for the classical and best metaheuristic algorithms. The parameters considered for evaluating the performance of each method are the ability of the corresponding algorithm to find the global optimal solution and its computational effort.

Table 7: Algorithms' performance – 45 bus system

Parameter	Benders	B&B	Enhanced PSO
Bus 1, Size 1 (MVA)	(378, 75)	(378, 67)	(378, 75)
Bus 2, Size 2 (MVA)	(433, 92)	(430, 150)	(433, 92)
J value	0.9174	1.0170	0.9174
Voltage deviation (J_1)	0.1824	0.1819	0.1824
Time (sec)	18,611	846	666
Power flows	63,095	2,155	2,000

Considering the ability of the algorithms to find the global optimal solution, Enhanced-PSO and Bender's decomposition, are able to find the best solution. On the other hand, the B&B algorithm gets trapped in a local minimum.

Concerning the computational effort, the number of fitness function evaluations for Benders' decomposition is 31.5 times larger than the Enhanced-PSO, with the resultant increase in computational time. Nevertheless, both algorithms require only a fraction of the total computational effort required by the exhaustive search, 0.17% and 0.005% for Benders, decomposition and Enhanced-PSO, respectively.

7. CONCLUSIONS

This paper compares several optimization algorithms applied to the problem of optimal allocation of FACTs devices in the power system: classical approaches such as Bender's decomposition and Branch and Bound (B&B) algorithms, and metaheuristic techniques such as Genetic Algorithm (GA), Particle Swarm Optimization (PSO), Enhanced-PSO and Bacterial foraging Algorithm (BFA).

Emphasis is placed on aspects of the optimization process that tend to be overlooked in the literature:

Convergence into feasible regions: for this type of application the feasible region is reduced, scattered and non-convex, therefore special consideration has to be given to the exploratory capabilities of the optimization algorithms. Enhanced-PSO algorithm is introduced to show the importance of this aspect: with simple rules to enhance the initial exploration of the problem hyperspace, this algorithm is capable of finding feasible solutions in 100% of the cases and twice as fast as compared to its closest competitor, the BFA algorithm, and 30 times faster than the canonical PSO.

Statistical analysis of algorithm's performance: performance of metaheuristic techniques is mostly analyzed using parameters, such as average value and standard deviation, which assume the data to be normally distributed. This paper shows that there are cases when the normality assumption does not hold. Weibull analysis is presented as an example of how statistical tools correctly applied in those cases can lead to interesting conclusions about the underlying search mechanism of metaheuristic algorithms.

Global Optimality: until now there is no proof that metaheuristic algorithms provide global optimality. This paper analyzes this aspect using a simple but realistic case study of optimal STATCOM allocation considering steady state and economic criteria. An exhaustive search is carried out on a 45 bus system to find the global optimum of the problem, and then statistical results are obtained for different optimization algorithms. The algorithm with the best performance is capable of finding the global optimum at least once over 50 trials, and in at least 70% of the time, the degree of sub-optimality is less than 10%.

Scalability of metaheuristic algorithms: scalability is investigated using as an example the Enhanced-PSO algorithm. Results are obtained for the IEEE 118 bus system and compared with the 45 bus system. Considering both, the convergence to feasible solutions and the degree of sub-optimality of the optimal solutions found, there is evidence that indicates that the performance of the algorithm is not affected by the size of the system.

Classical versus metaheuristic approaches: the classical approaches, Bender's decomposition and B&B are compared with the Enhanced-PSO considering the capability of the algorithms in finding the global optimal solution and their computational effort. Bender's decomposition and Enhanced PSO are capable of finding the global optimum however B&B becomes trapped in a local optimal point. For all algorithms, the number of power flow computations is small (compared to the exhaustive search), but a comparison between them favors the metaheuristic algorithm since Bender's decomposition takes 30.5% more computational effort than the Enhanced –PSO.

A final concluding remark is that, at present, there is no optimization method that universally outperforms all others. The selection of an algorithm is problem dependent, and this paper makes a particular effort in showing different aspects that should be considered while choosing an optimization method for solving the problem of allocating FACTS devices.

ACKNOWLEDGEMENTS

This work has been partly supported by NSF Grants ECS #0524183 and ECCS #0348221.

REFERENCES

[1] D. Wanhong, T. Lie, "Optimal compensation of variable series capacitors for improved economic dispatch in power systems," Proc. of the IEEE International Conference on Energy Management and Power Delivery (EMPD) 1995,Vol. 2, Nov. 1995, pp. 732-737.

[2] F. Lima, F. Galiana, I. Kockar and, J. Munoz, "Phase shifter placement in large-scale systems via mixed integer linear programming," *IEEE Transactions on Power Systems*, Vol.18, no.3, Aug.2003, pp.1029-1034.

[3] A. Sharma, S. Chanana, S. Parida, "Combined optimal location of FACTS controllers and loadability enhancement in competitive electricity markets using MILP," Proc. of the IEEE Power Engineering Society General Meeting, 2005. Vol. 1, Jun. 2005, pp. 670–677.

[4] N. Yorino, E. El-Araby, H. Sasaki, S. Harada, "A new formulation for FACTS allocation for security enhancement against voltage collapse," *IEEE Transactions on Power Systems*, Vol. 18, no. 1, Feb. 2003, pp. 3-10.

[5] E. El-Araby, N. Yorino, H. Sasaki, "A comprehensive approach for FACTS devices optimal allocation to mitigate voltage collapse," Proc. of the IEEE Transmission and Distribution Conference and Exhibition 2002: Asia Pacific. Vol. 1, Oct. 2002, pp. 62-67.

[6] E. De Oliveira, J. Marangon Lima, K. De Almeida, "Allocation of FACTS devices in hydrothermal systems," *IEEE Transactions on Power Systems*, Vol. 15, no. 1, Feb. 2000, pp. 276-282.

[7] S. Gerbex, R. Cherkaoui, A. Germond, "Optimal location of FACTS devices to enhance power system security," Proc. of the IEEE Power Tech Conference Proceedings, 2003 Bologna, Vol. 3, Jun. 2003, pp. 7-14.

[8] S. Gerbex, R. Cherkaoui, A. Germond, "Optimal location of multi-type FACTS devices in a power system by means of genetic algorithms," *IEEE Transactions on Power Systems*, Vol. 16, no. 3, Aug. 2001, pp.537–544.

[9] L. Ippolito, P. Siano, "Selection of optimal number and location of thyristor-controlled phase shifters using genetic based algorithms," Proc. of the IEE Generation, Transmission and Distribution, Vol. 151, no. 5, Sept. 2004, pp. 630–637.

[10] D. Radu, Y. Besanger, "A multi-objective genetic algorithm approach to optimal allocation of multi-type FACTS devices for power systems security," Proc. of the IEEE Power Engineering Society General Meeting, 2006, Jun. 2006, pp. 8-16.

[11] H. Shaheen, G. Rashed, S. Cheng, "Optimal location and parameters setting of unified power flow controller based on evolutionary optimization techniques," Proc. of the IEEE Power Engineering Society General Meeting, 2007. Jun. 2007, pp. 1-8.

[12] M. Saravanan, S. Slochanal, P. Venkatesh, P. Abraham, "Application of PSO technique for optimal location of FACTS devices considering system loadability and cost of installation," Proc. of the IEEE 7th International Power Engineering Conference (IPEC) 2005. Vol. 2, Dec. 2005, pp. 716-721.

[13] H. Mori, Y. Maeda, "A hybrid method of EPSO and TS for FACTS optimal allocation in power systems," Proc. of the IEEE International Conference on Systems, Man and Cybernetics (ICSMC '06), 2006. Vol. 3, Oct. 2006, pp. 1831-1836.

[14] W. Ongsakul, P. Jirapong, "Optimal placement of multi-type FACTS devices by hybrid TS/SA approach," Proc. of the IEEE International Symposium on Circuits and Systems (ISCAS), Vol. 3, May 2003, pp. III-375 - III-378.

[15] J. Hao, L. Shi, Ch. Chen, "Optimising location of unified power flow controllers by means of improved evolutionary programming," Proc. of the IEE Generation, Transmission and Distribution, Vol. 151, no. 6, Nov. 2004, pp.705–712.

[16] W. Ongsakul, P. Jirapong, "Optimal allocation of FACTS devices to enhance total transfer capability using evolutionary programming," Proc. of the IEEE International Symposium on Circuits and Systems (ISCAS), Vol. 5, May 2005, pp. 4175-4178.

[17] D. Bertsimas and J. N. Tsitsiklis, *Introduction to linear optimization*, Athena Scientific Series in Optimization and Neural Computation, 1997.

[18] S Mohagheghi, Y. del Valle, G.K. Venayagamoorthy and R.G. Harley, "A Proportional-Integrator Type Adaptive Critic Design Based Neurocontroller for a Static Compensator in a Multimachine Power System". *IEEE Transactions on Industrial Electronics.* Vol. 54, No.1, February 2007, pp. 86-96.

[19] B. Kumar, S. Singh, S. Srivastava, "Placement of FACTS controllers using modal controllability indices to damp out power system oscillations," IET Generation, Transmission & Distribution, Vol. 1, no. 2, March 2007, pp. 209-217.

[20] G.L. Nemhauser and L.A. Wolsey, *Integer and combinatorial optimization*, Wiley-Interscience, New York, 1999.

[21] K. G. Murty, *Operations research: deterministic optimization models*, Prentice Hall, 1995.

[22] D. Goldberg, *Genetic algorithms in search, optimization and machine learning*. Addison-Wesley Pub. Co. 1989.

[23] L Schmitt, "Theory of genetic algorithms," Theoretical Computer Science (259), 2001, pp. 1-61.

[24] Y. del Valle, M. Digman, A. Gray, J. Perkel, G. Venayagamoorthy, and R. Harley, "Enhanced Particle Swarm Optimizer for Power System applications", Proc. of the IEEE Swarm Intelligence Symposium, 2008 (SIS 2008). St. Louis, Missouri, September 21-23, 2008.

[25] R. Eberhart, Y.Shi and J. Kennedy, *Swarm Intelligence*. San Francisco, CA: Morgan Kaufmann, 2001.

[26] Y. del Valle, G.K. Venayagamoorthy, S. Mohagheghi,, J. C. Hernandez, and R.G. Harley, "Particle Swarm Optimization: Basic Concepts, Variants and Applications in Power System". *IEEE Transactions on Evolutionary Computation*, Vol. 12, No. 2, April 2008, pp: 171-195.

[27] T.K. Das, G.K. Venayagamoorthy, "Bio-inspired Algorithms for the Design of Multiple Optimal Power System Stabilizers: SPPSO and BFA", Conference Record of the 2006 IEEE Industry Applications Conference, 41st IAS Annual Meeting. Vol. 2, 8-12 Oct. 2006, pp:635 – 641.

[28] K. M. Passino, "Biomimicry of bacterial foraging for distributed optimization and control," Control System Magazine, IEEE, vol. 22, Issue 3, pp. 52-67, June 2002.

[29] R. B. Abernethy, *The New Weibull Handbook*, North Palm Beach, FL, Robert B. Abernethy, 1993.

[30] The IEEE 118 Bus Test System. [Online]. Available: http://www.ee.washington.edu/research/pstca/.

Modelling of a Spatially Correlated MIMO Wireless Channel

B.B. Varghese* and B.T. Maharaj**

** Dept. of Electrical, Electronic and Computer Eng. Univ. of Pretoria, Lynnwood Road, South Africa, 0002, e-mail: benubobben@yahoo.com*
*** Dept. of Electrical Electronic and Computer Engineering, Univ. of Pretoria, Lynnwood Road, South Africa, e-mail:sunil.maharaj@up.ac.za*

Abstract: The channel capacity of a wireless communication system is greatly increased with the usage of multiple antennas at both the transmitter and receiver as long as the environment provides sufficient scattering. This paper shows a new geometric MIMO channel model that has taken the path loss parameter into account, as well as non-isotropic scattering at both ends of the radio link. Separate transmit and receive correlation functions are derived in a compact closed format, which includes some key parameters, such as distance between transmitter and receiver, antenna element spacing and degree of scattering. The capacity of the MIMO fading channel with varying number of antenna elements, distance between transmitter and receiver, various environments, varying signal to noise ratio at the receiver, varying the antenna element spacing at the transmitter and the degree of scattering at transmitter and receiver are investigated and shown for this model.

Key words: correlation, fading channels, MIMO, non-isotropic scattering, path loss.

1. INTRODUCTION

Multiple Input Multiple Output (MIMO) systems employ multiple antennas at both transmitter and receiver and were firstly reported by Teletar, [1] and Foschini, Gans, [2] that can be dated back to 1995. It was shown that MIMO channels could offer larger gains in capacity than the traditional Single Input Single Output (SISO) channel using the Shannon Capacity formula.

The need for high data rate in wireless communications coupled with the problem of power and bandwidth restrictions, as well as the multipath fading channel has increased profusely in the recent years. Due to this, much attention has been given to research of antenna arrays in mobile and fixed wireless communication systems.

Many research papers have been presented on MIMO systems in areas as diverse as channel modeling, information theory and coding, signal processing, antenna design and multi- antenna cellular design for fixed and mobile wireless communications. This paper is an extended version of [3] that is based on MIMO channel modeling which investigates the effects of correlation and path loss on a multiple element antenna transmission and reception system. An overview of the different models for MIMO propagation is shown in [4]

Some of these models can be categorized into two different groups based on the location of the scatterers. The first group consists of scatterers present only at the User (receiver) as shown in [5], [6] and [7] while the second has scatterers situated at the Base station and the User [8].

The most common communication model is based on the first group where the base station is in an elevated position and lies unobstructed by local scatterers. The User is situated at ground level where there are a large number of local scatterers due to the different objects (like vegetation, landscape, buildings, etc) surrounding the User.

The second group is another communication model that has recently been given some attention. In this group, both the base station and user are considered to be surrounded by a large number of local scatterers. Even though the base station is elevated, it can also be obstructed by tall buildings, trees or hilly areas.

Much research has been done on the first group of models, by investigating the effects of correlation on a multiple element antenna transmission and reception system while only a few have been done on the second group model.

This paper presents a new geometric model for a fixed MIMO channel, which is almost similar to the second group where there is non-isotropic scattering at both the transmitter and receiver. This model has considered different parameters together that will affect the correlation in a MIMO channel. All the previous models have only investigated a few of these parameters and not all of them.

The different parameters considered are the inclusion of the path loss parameter, n, the distance between the transmitter and receiver and the scatterers present at both transmitter and receiver. We consider a circular ring of scatterers to surround the user as shown in [9], while a ring of scatterers surrounds the base station. Also path loss is considered, which depends upon the distance between the transmitter and receiver. It also depends upon the environment, which may be urban, rural, indoor

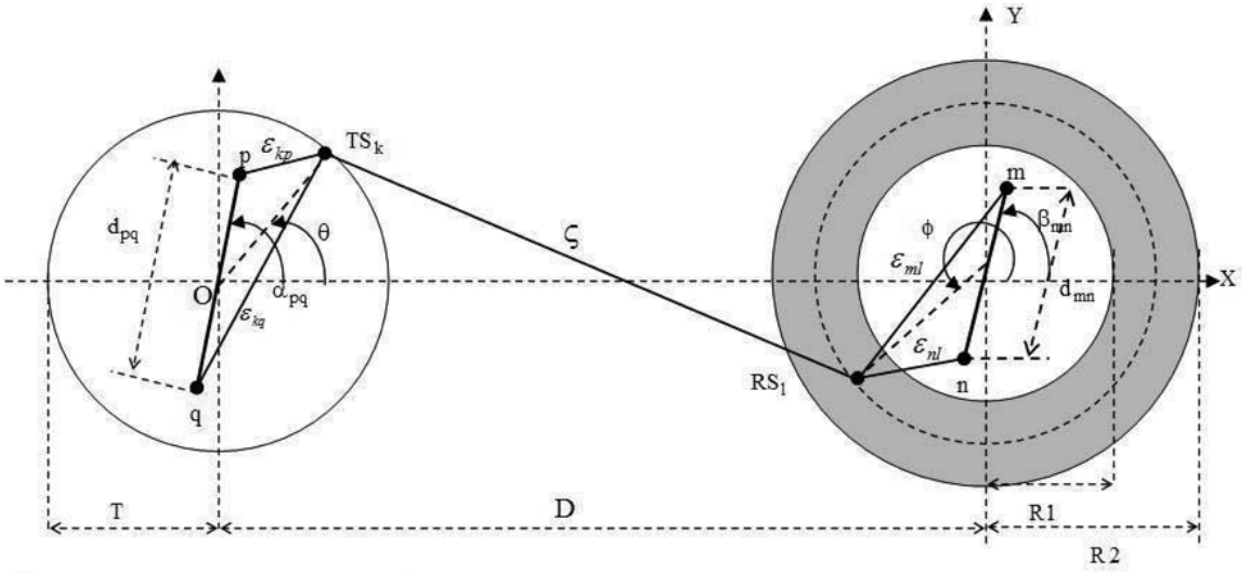

Figure 1: Geometric Model for a 2 x 2 MIMO channel

or outdoor [10]. Separate transmit and receive antenna correlation functions are derived from this model. Capacities for this model for different environments under different assumptions are presented.

This paper is organized as follows. The geometric MIMO channel model is shown and described in section 2 with its corresponding cross correlation functions that has been derived in section 3. The calculation of the capacity and the simulation results are presented in section 4 and finally in section 5, conclusions are drawn.

2. THE NEW MIMO CHANNEL MODEL

Consider a narrowband single user communication system with two transmit and two receive omni-directional antenna elements as shown in Fig 1. No line of sight (NLOS) is assumed. Since the user or receiver is subjected to more scatterers that may not necessary lie in a ring format, it is assumed that the scatterers can be located at any point on the circular ring. The distance of the scatterers on the circular ring to the user ranges between R1 and R2. Both the transmitter and receiver are assumed to be fixed and the distance between them is D with α_{pq} and β_{mn} as the angles the antenna arrays form with the horizontal axis. The input / output relation of this MIMO system can be written as

$$\bar{y}(t) = H(t)\bar{x}(t) + \bar{n}(t) \qquad (1)$$

Where: $\bar{x}(t)$ is the transmit vector that contains elements $x_j(t)$, which denotes the signal transmitted from antenna $j = \{1,...,n_T\}$, where n_T is the number of transmitter antenna elements and in this case $n_T = 2$.

$\bar{y}(t)$ is the receive vector that contains elements $y_i(t)$, which denotes the signals received by antenna $i = \{1,...,n_R\}$, where n_R is the number of receiver antenna elements and in this case $n_R = 2$.

$\bar{n}(t)$ is the noise vector that contains elements $n_i(t)$, which denotes the additive white Gaussian noise (AWGN) at the receiver antenna.

$H(t)$ is a $n_R \times n_T$ channel matrix of complex path gains $H_{ij}(t)$ between transmit antenna j and receive antenna i.

Certain assumptions are made for Fig.1, which are similar to [7]-[9]. It is assumed that K scatterers lie on the ring of radius T at the base station where the k^{th} transmit scatterer is denoted by TS_k. Similarly L scatterers lie on the circular ring of radius $R1 \le R \le R2$ where the 1^{th} scatterer is denoted by RS_l. Each scatterer introduces a gain and phase shift and is assumed to be dependent on the direction of the ray's arrival. The gain and phase shift introduced by RS_l from a ray received from TS_k is different from that introduced by another ray received from another scatterer, say TS_k'.

It is also assumed that rays from different antenna elements arrive at a scatterer at the same angle and so for a particular scatterer, the gain and phase shift is the same for rays coming from different antenna elements. The joint gain and phase shift of TS_k and RS_l is denoted by g_{lk} and ψ_{lk}.

Since K is the number of independent scatterers surrounding the base station and L is the number of independent scatterers surrounding the user, it can be assumed that as K and L tends to infinity.

$$\frac{1}{KL}\sum_{k=1}^{K}\left\{\sum_{l=1}^{L}E\left[g_{lk}^{2}\right]\right\}=1 \tag{2}$$

The channel gain h_{mp} for the link between base station antenna element p and user antenna element m is given by the equation:

$$h_{mp}(t)=\sqrt{\Omega_{mp}}\lim_{K,L\to\alpha}\frac{1}{\sqrt{KL}}\sum_{k=1}^{K}\sum_{l=1}^{L}g_{lk}(d)^{-n/2} \times\exp\left[j\psi_{lk}-\frac{j2\pi}{\lambda}\left(\varepsilon_{kp}+\varsigma+\varepsilon_{ml}\right)\right] \tag{3}$$

Here h_{mp} is a Rayleigh fading process obtained from the central limit theorem which implies that h_{mp} is a low pass, zero mean, complex Gaussian random process, similar to [11] and n is the path loss parameter depending upon the environment as shown in [10, page 139]. The power transferred through this link is Ω_{mp} and $\varepsilon_{kp}, \varsigma$ and ε_{ml} are the distances as shown in Fig.1. The distance, d traveled by the ray can be written as:

$$d=T+\varsigma+R \tag{4}$$

From the diagram, ς can be calculated under certain assumptions. Consider the triangle ΔOTS_kRS_l and assume $D \gg R1, R2$, then the distance $ORS_l \approx (D-R)$ Applying the law of cosines:

$$\varsigma^2=T^2+(D-R)^2-2T(D-R)\cos\mu_T \tag{5}$$

Hence ς can be written as:

$$\varsigma=\sqrt{T^2+(D-R)^2-2T(D-R)\cos\mu_T} \tag{6}$$

Where $\mu_T\in(-\pi,\pi)$ is the mean angle at which the scatterers are distributed on the ring.

3. DERIVATION OF THE CROSS CORRELATION FUNCTION

A joint space-time cross correlation function is derived from the model shown in Fig.1 in a manner that is similar to [6]. The correlation between two links mp and nq for a time delay τ can be defined as:

$$\rho_{mp,nq}(t,\tau)=E\left[h_{mp}(t)h_{nq}^{*}(t+\tau)\right]/\sqrt{\Omega_{mp}.\Omega_{nq}} \tag{7}$$

Where Ω_{mp} is the power transferred from the transmitter antenna p to the receiver antenna m and Ω_{nq} is the power transferred from the transmitter antenna q to the receiver antenna n. Here * indicates the complex conjugate and

$$h_{nq}^{*}(t+\tau)=\sqrt{\Omega_{nq}}\lim_{K,L\to\alpha}\frac{1}{\sqrt{KL}}\sum_{k=1}^{K}\sum_{l=1}^{L}g_{lk}(d)^{-n/2} \times\exp\left[-j\psi_{lk}+\frac{j2\pi}{\lambda}\left(\varepsilon_{kq}+\varsigma+\varepsilon_{nl}\right)\right] \tag{8}$$

After substitutions, (7) gives:

$$\rho_{mp,nq}(t,\tau)=\lim_{K,L\to\alpha}\frac{1}{KL}\sum_{k=1}^{K}\left\{\sum_{l=1}^{L}E\left[g_{lk}^{2}\right](d)^{-n}\right\} \times\exp\left(\frac{-j2\pi}{\lambda}\left(\varepsilon_{kp}+\varepsilon_{ml}-\varepsilon_{kq}-\varepsilon_{nl}\right)\right) \tag{9}$$

Since the receiver is assumed to be fixed and the channel is in a quasi-static state, it can be written:

$$\rho_{mp,nq}(t,\tau)=\rho_{mp,nq}(\tau)=\rho_{mp,nq} \tag{10}$$

As K and L approach infinity, (3) can be written as [9], [12]:

$$\lim_{K,L\to\alpha}\frac{E\left|g_{lk}^{2}\right|}{KL}(d)^{-n} =(d)^{-n}p(\theta)p(\phi,R)d\theta d\phi dR \tag{11}$$

Where $p(\theta)$ and $p(\phi,R)$ are the probability distributions of both the transmit and receive scatterers. Substituting the above relation in (9):

$$\rho_{mp,nq}=(d)^{-n}\int_{R1}^{R2}\int_{-\pi}^{\pi}\int_{-\pi}^{\pi}\exp\left\{-\frac{j2\pi}{\lambda}\left(\varepsilon_{\theta p}+\varepsilon_{m\phi}-\varepsilon_{\theta q}-\varepsilon_{n\phi}\right)\right\} \times p(\theta)p(\phi,R)d\theta d\phi dR \tag{12}$$

$\varepsilon_{\theta p}$ is the distance from p to the ring of transmitter scatterers TS_k at an angle θ from the ring centre. All the other terms are defined in the same manner.

By using the law of cosines, (12) can be calculated numerically from the following equations:

$$\varepsilon_{\theta p}^2 = \frac{d_{pq}^2}{4} + T^2 - d_{pq} T \cos(\alpha_{pq} - \theta)$$

$$\varepsilon_{\theta q}^2 = \frac{d_{pq}^2}{4} + T^2 + d_{pq} T \cos(\alpha_{pq} - \theta)$$

$$\varepsilon_{m\phi}^2 = \frac{d_{mn}^2}{4} + R^2 - d_{mn} R \cos(\phi - \beta_{mn})$$

$$\varepsilon_{n\phi}^2 = \frac{d_{mn}^2}{4} + R^2 + d_{mn} R \cos(\phi - \beta_{mn}) \quad (13)$$

Where d_{pq} is the antenna element spacing at the transmitter and d_{mn} is the antenna element spacing at the receiver.

Assuming the following:

$T >> d_{pq}, R >> d_{mn}$, $\lim_{x \to 0} \sin x \approx x$ and

$\lim_{x \to 0} \sqrt{1+x} \approx 1 + \frac{x}{2}$,

the equations in (11) can be simplified to:

$$\varepsilon_{\theta p} \approx T - \frac{d_{pq}}{2} \cos(\alpha_{pq} - \theta)$$

$$\varepsilon_{\theta q} \approx T + \frac{d_{pq}}{2} \cos(\alpha_{pq} - \theta)$$

$$\varepsilon_{m\phi} \approx R - \frac{d_{mn}}{2} \cos(\phi - \beta_{mn})$$

$$\varepsilon_{n\phi} \approx R + \frac{d_{mn}}{2} \cos(\phi - \beta_{mn}) \quad (14)$$

Assuming $p(\phi, R) = p(\phi)p(R)$, the scatterer distribution used here for the transmitter, $p(\theta)$ and the receiver, $p(\phi)$ is the von Mises PDF [13] which provides closed form solutions and is given by

$$p(\theta) = \frac{1}{2\pi . I_0(\kappa_T)} \exp[\kappa_T \cos(\theta - \mu_T)]$$

$$p(\phi) = \frac{1}{2\pi . I_0(\kappa_R)} \exp[\kappa_R \cos(\phi - \mu_R)] \quad (15)$$

where $\theta, \phi \in (-\pi, \pi)$, κ_T and κ_R are the scattering parameters at the transmitter and receiver, μ_T and μ_R are the mean angles at which the scatterers are assumed to be distributed on the ring and $I_0(.)$ is the zero order modified Bessel function.

By splitting the terms in (12) into two different groups, one containing θ that represents the transmitter (TX) correlation, $\rho_{p,q}^{TX}$ and the other containing ϕ that represents the receiver (RX) correlation, $\rho_{m,n}^{RX}$, the joint antenna correlation can be written as [6], [7] & [8]:

$$\rho_{mp,nq} \approx \rho_{pq}^{TX} . \rho_{mn}^{RX} \quad (16)$$

Taking the attenuation factor, n in the TX side, the separate transmit and receive antenna correlation is written as

$$\rho_{pq}^{TX} = (d)^{-n} \int_{-\pi}^{\pi} \exp\left\{-\frac{j2\pi}{\lambda}\left(\varepsilon_{\theta p} - \varepsilon_{\theta q}\right)\right\} p(\theta) d\theta$$

$$\rho_{mn}^{RX} = \int_{R1}^{R2} \int_{-\pi}^{\pi} \exp\left\{-\frac{j2\pi}{\lambda}\left(\varepsilon_{m\phi} - \varepsilon_{n\phi}\right)\right\} p(\phi) p(R) d\phi dR \quad (17)$$

Substituting (14) in (17):

$$\rho_{pq}^{TX} = (d)^{-n} \int_{-\pi}^{\pi} \exp\left\{-\frac{j2\pi}{\lambda}\left(-d_{pq} \cos(\alpha_{pq} - \theta)\right)\right\} p(\theta) d\theta$$

$$\rho_{mn}^{RX} = \int_{R1}^{R2} \int_{-\pi}^{\pi} \exp\left\{-\frac{j2\pi}{\lambda}\left(-d_{mn} \cos(\phi - \beta_{mn})\right)\right\} p(\phi) p(R) d\phi dR \quad (18)$$

After further simplifications:

$$\rho_{pq}^{TX} = (d)^{-n} \int_{-\pi}^{\pi} \exp\left\{\frac{j2\pi}{\lambda} d_{pq} \cos(\alpha_{pq} - \theta)\right\} p(\theta) d\theta$$

$$\rho_{mn}^{RX} = \int_{R1}^{R2} \int_{-\pi}^{\pi} \exp\left\{\frac{j2\pi}{\lambda} d_{mn} \cos(\phi - \beta_{mn})\right\} p(\phi) p(R) d\phi dR \quad (19)$$

Substituting (15) in (19):

$$\rho_{pq}^{TX} = \frac{(d)^{-n}}{2\pi I_0(\kappa_T)} \int_{-\pi}^{\pi} \exp\left\{\frac{j2\pi}{\lambda} d_{pq} \cos(\alpha_{pq} - \theta)\right\} \times \exp\{\kappa_T \cos(\theta - \mu_T)\} d\theta$$

$$\rho_{mn}^{RX} = \frac{1}{2\pi I_0(\kappa_R)} \int_{R1}^{R2} \int_{-\pi}^{\pi} \exp\left\{\frac{j2\pi}{\lambda} d_{mn} \cos(\phi - \beta_{mn})\right\} \times \exp\{\kappa_R \cos(\phi - \mu_R)\} p(R) d\phi dR \quad (20)$$

Using the formula:

cos (A-B) = cosA.cosB + sinA.sinB, the equation (20) can be written as:

$$\rho_{pq}^{TX} = \frac{(d)^{-n}}{2\pi I_0(\kappa_T)} \times \int_{-\pi}^{\pi} \exp\left\{\begin{array}{l} \frac{j2\pi}{\lambda} d_{pq} \left[\cos\alpha_{pq} . \cos\theta + \sin\alpha_{pq} . \sin\theta\right] \\ + \kappa_T \left[\cos\theta . \cos\mu_T + \sin\theta \sin\mu_T\right] \end{array}\right\} d\theta$$

$$\rho_{mn}^{RX} = \frac{1}{2\pi I_0(\kappa_R)} \int_{R1}^{R2} \times \int_{-\pi}^{\pi} \exp\left\{ \begin{array}{l} \frac{j2\pi}{\lambda} d_{mn} [\cos\phi.\cos\beta_{mn} + \sin\phi.\sin\beta_{mn}] \\ + \kappa_R [\cos\phi.\cos\mu_R + \sin\phi.\sin\mu_R] \end{array} \right\} p(R) d\phi dR \quad (21)$$

Further simplifications give:

$$\rho_{pq}^{TX} = \frac{(d)^{-n}}{2\pi I_0(\kappa_T)} \times \int_{-\pi}^{\pi} \exp\left\{ \begin{array}{l} \cos\theta \left[\frac{j2\pi}{\lambda} d_{pq} \cos\alpha_{pq} + \kappa_T \cos\mu_T \right] \\ + \sin\theta \left[\frac{j2\pi}{\lambda} d_{pq} \sin\alpha_{pq} + \kappa_T \sin\mu_T \right] \end{array} \right\} d\theta$$

$$\rho_{mn}^{RX} = \frac{1}{2\pi I_0(\kappa_R)} \int_{R1}^{R2} \times \int_{-\pi}^{\pi} \exp\left\{ \begin{array}{l} \cos\phi \left[\frac{j2\pi}{\lambda} d_{mn} \cos\beta_{mn} + \kappa_R \cos\mu_R \right] \\ + \sin\phi \left[\frac{j2\pi}{\lambda} d_{mn} \sin\beta_{mn} + \kappa_R \sin\mu_R \right] \end{array} \right\} p(R) d\phi dR \quad (22)$$

Making use of the integration rule in [14] (page 336, equation 3.338-4):

$$\int_{-\pi}^{\pi} \exp(y\sin x + z\cos x) dx = 2\pi I_0(\gamma) \quad (23)$$

where $\gamma = \sqrt{y^2 + z^2}$ and the trigonometric rule $\cos^2 A + \sin^2 A = 1$, then (22) can be written as:

$$\rho_{pq}^{TX} = \frac{(d)^{-n}}{I_0(\kappa_T)} \times I_0 \left[\left(\kappa_T^2 + \left(\frac{j2\pi}{\lambda} d_{pq} \right)^2 + j\frac{4\pi}{\lambda} d_{pq} \kappa_T \cos(\mu_{TX} - \alpha_{pq}) \right)^{\frac{1}{2}} \right]$$

$$\rho_{mn}^{RX} = \frac{1}{I_0(\kappa_R)} \times I_0 \left[\left(\kappa_R^2 + \left(\frac{j2\pi}{\lambda} d_{mn} \right)^2 + j\frac{4\pi}{\lambda} d_{mn} \kappa_R \cos(\mu_{RX} - \beta_{mn}) \right)^{\frac{1}{2}} \right] \times \frac{2}{\left(R_2^2 - R_1^2 \right)} \int_{R1}^{R2} R dR \quad (24)$$

After further simplification, the TX correlation is given by:

$$\rho_{pq}^{TX} = \frac{(d)^{-n}}{I_0(\kappa_T)} I_0 \left[\left(\kappa_T^2 - c_{pq}^2 + j2c_{pq}\kappa_T \cos(\mu_{TX} - \alpha_{pq}) \right)^{\frac{1}{2}} \right] \quad (25)$$

Where $c_{pq} = \frac{2\pi d_{pq}}{\lambda}$ and κ_T is the scattering parameter at the transmitter.

Assuming $p(R) = 2R / \left(R_2^2 - R_1^2 \right)$ taken from [9], the RX correlation is given by

$$\rho_{mn}^{RX} = \frac{1}{I_0(\kappa_R)} I_0 \left[\left(\kappa_R^2 - b_{mn}^2 + j2b_{mn}\kappa_R \cos(\mu_{RX} - \beta_{mn}) \right)^{\frac{1}{2}} \right] \times \frac{2}{\left(R_2^2 - R_1^2 \right)} \int_{R1}^{R2} R dR \quad (26)$$

Where $b_{mn} = \frac{2\pi d_{mn}}{\lambda}$ and κ_R is the scattering parameter at the receiver.

By using the above closed form expressions in (25) and (26), one is able to determine some of the model characteristics as shown in the next section.

4. MODEL RESULTS

Let $\overline{U}$ be a $n_R \times n_T$ matrix of random, independent and zero mean complex Gaussian variates with unit variance and $\overline{X}$ be the $n_T \times n_T$ matrix of the transmit antenna correlation with matrix elements calculated from (25). Then the desired transmit antenna correlation is calculated by $x = \overline{U}\sqrt{\overline{X}}$. The channel matrix $\overline{H}$, between the transmitter and receiver can be calculated by $\overline{H} = x\sqrt{\overline{Y}}$, where $\overline{Y}$ is the $n_R \times n_R$ matrix of the receive antenna correlation with matrix elements calculated from (26).

From [1] and [2], the normalized channel Capacity for a particular realization H is given by

$$C = \log_2 \det \left[I_{n_R} + \frac{SNR}{n_T} \overline{HH}^H \right] \text{ b/s/Hz} \quad (27)$$

Where I_{n_R} is the $n_R \times n_R$ identity matrix, SNR is the average signal to noise ratio at the receiver, $\overline{H}^H$ is the conjugate transpose of $\overline{H}$ and $\det[.]$ is the determinant.

Simulations were done for this model for the following

general parameters SNR = 20dB, transmit carrier frequency = 2.4GHz (so $\lambda = 0.125$m), $\alpha_{pq} = \pi/2, \beta_{mn} = \pi/4$, $\kappa_R = 50$, R1=1m, R2=2m, T=1m, $\mu_{TX} = 0$, $\mu_{RX} = \pi$ and the antenna spacing for transmitter and receiver are $d_{mn} = d_{pq} = 0.3\lambda$.

The simulation in fig. 2 is the complementary cumulative distribution function (ccdf) versus capacity for various number of transmit and receive antenna elements. Here $\kappa_T = 10$, D =10m and n = 2.

Observing the figure, one can see that the capacity increases as the number of antennas increases. This graph shows the effect of scattering and the number of antenna elements present at both the transmitter and receiver. As the number of antenna elements goes on increasing, the capacity increase intervals gradually decreases.

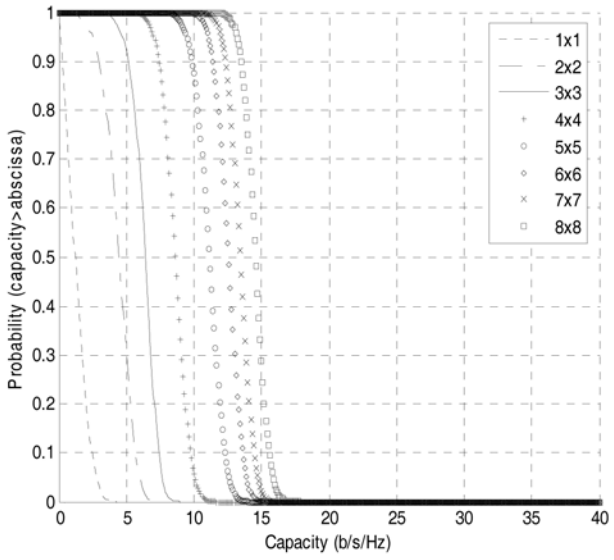

Figure 2. ccdf vs. capacity for varying antenna elements, $n_R x n_T$

The distance, D between the transmitter and receiver is varied as shown in fig 3. Here $\kappa_T = 10$ $\kappa_R = 50$ n=2 and $n_T = n_R = 8$.

It can be observed that as the distance between the transmitter and receiver increases, the capacity decreases. From the figure, one can see that the capacity varies most significantly when the distance between transmitter and receiver ranges from 5m to 10 m that is 5m < D < 10m and it gradually decreases in variation when the distance between transmitter and receiver is greater than 10m that is D > 10m at regular intervals of 5m.

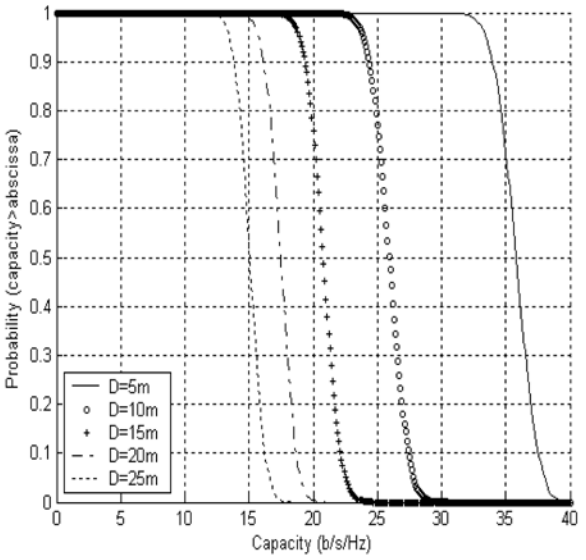

Figure 3. ccdf vs. capacity for varying distance between transmitter and receiver.

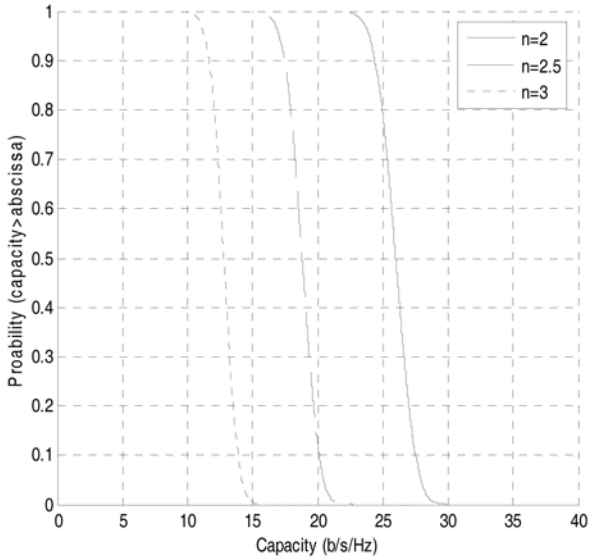

Figure 4. ccdf vs. capacity for varying path loss exponent (n).

For $\kappa_T = 10$, D=10 and $n_T = n_R = 8$, figure 4 shows the effect of the variation in the path loss exponent n, which depends on the environment used [10, page139]. For n=2 represents free space and for n between 2 to 6 represents either an urban area or an indoor no line of sight (NLOS). For n=1.6 represents an indoor line of sight (LOS) and the capacity will obviously be higher for the plotted values of n. This is not shown as this channel model is for a Rayleigh case.

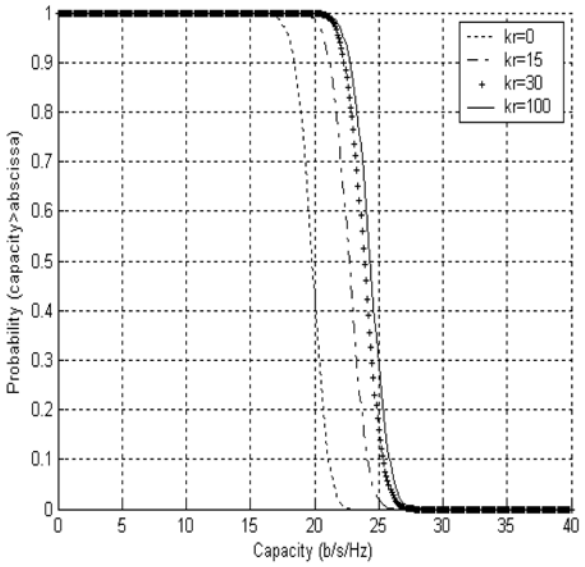

Figure 5. ccdf vs. capacity for varying scattering parameter at receiver.

Figure 5 shows the effect of the variation in the receiver scattering parameter κ_R. Here $\kappa_T = 5$, D=10m, $n_T = n_R = 8$ and n=2. For a 90% probability, the capacity increases by 4.5b/s/Hz for a κ_R increase from 0 to 30 and by only 0.5b/s/Hz for a κ_R increase from 30 to 100. This shows that the degree of scattering plays an important role in the enhancement of capacity for a MIMO system up to a certain point, where upon any further richness in scatterers has negligible effect on the capacity.

It was also found that if one varies the scattering parameter at the transmitter, κ_T, the capacity also increases for the same outage probability.

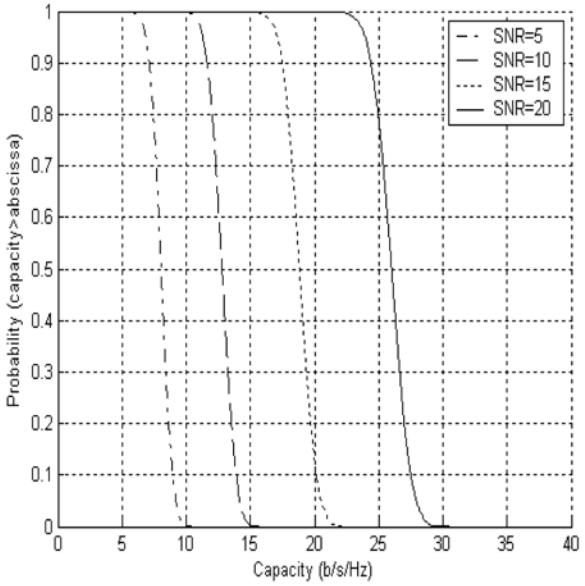

Figure 6. ccdf vs. capacity for varying signal to noise ratio (SNR) parameter.

In Figure 6, the effect of the variation of the signal to noise ratio (SNR) is shown, which is one of the most common and important parameter in a communication system. Here, $\kappa_T = 10$, $\kappa_R = 50$, D=10m, $n_T = n_R = 8$ and n=2. From the figure we can see as the signal to noise ratio increases, the capacity also increases as expected thus also validating the model. For a signal to noise ratio increase from 5dB to 10dB, the capacity increases by 5b/s/Hz for a 90% probability and from 10dB to 15dB, the capacity increases by 6b/s/Hz. The 15dB to 20dB signal to noise ratio increase shows a capacity increase of 7b/s/Hz for the same probability. This shows the effect of the signal to noise ratio on this channel model.

The effect of variation of the antenna element spacing at the transmitter is shown in fig 7. The SNR=20 dB, $\kappa_T = 10$, $\kappa_R = 50$, D=10m, $n_T = n_R = 8$, n=2 and $d_{mn} = 0.3\lambda$ was used in the computation. From the figure, one can see that as the antenna element spacing increases, the capacity automatically decreases to a certain extent. One observes that when $d_{pq} < 0.5\lambda$ and $d_{pq} > 0.8\lambda$, the capacity varies significantly. It was also found that when $d_{pq} > 1\lambda$, the capacity decreases very slightly, thus making it almost negligible.

It was also found that if one simultaneously varied the antenna spacing at the receiver, d_{mn}, the capacity decreases significantly for the same outage probability.

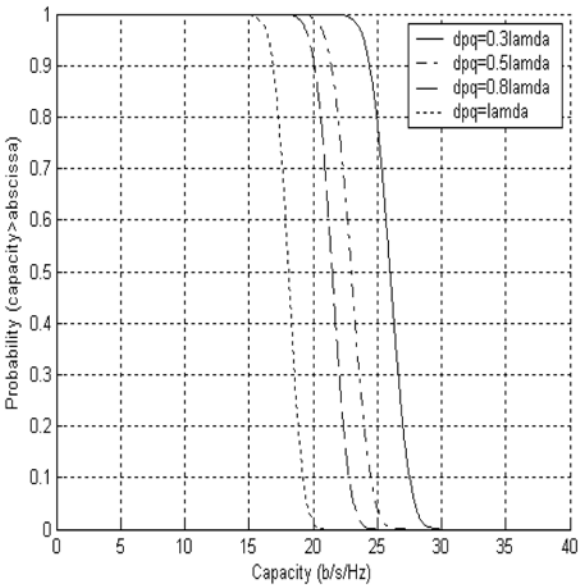

Figure 7. ccdf vs. capacity for varying antenna element spacing at the transmitter.

5. CONCLUSION

This model was developed for a fixed wireless indoor environment. A joint cross correlation function as well as separate transmit and receive correlation functions are derived. The effects of the number of antenna elements, the distance between the transmitter and receiver, the path loss exponent (environment), the signal to noise ratio (SNR), the degree of scattering at the receiver and the antenna element spacing at the transmitter are investigated and shown in the respective simulation graphs. From the results shown, it can be analyzed that the number of antenna elements, the signal to noise ratio and the distance between TX and RX has the most significant effect on the capacity.

This channel model was developed for separate transmit and receive correlation functions (Kronecker method). Further studies can be done by deriving a closed form joint correlation function for the same channel model by taking the same path loss exponent into account as well as the scattering at both ends of the radio link. Simulations can be plotted for the effect on capacity by varying the same parameters shown in this paper. They can then be compared with measured values [17] to show the more accurate method.

6. REFERENCES

[1] I. E. Telatar, "Capacity of multi-antenna Gaussian Channels," Tech. Rep. #BL0112170-950615-07TM, AT&T Bell Laboratories, 1995.

[2] G. J. Foschini and M. J. Gans, "On limits of wireless communication in a fading environment when using multiple antennas," *Wireless Personal Communications*, vol. 6, no. 3, pp.311-335, Kluwer Academic Publishers, March, 1998.

[3] B. B. Varghese and B. T. Maharaj, "A Spatially Correlated Model for MIMO Fading Channels," *Presented at the 12th ICT Wireless Comms and Technologies*, March 2005.

[4] K. Yu and B. Ottersten, "Models for MIMO propagation channels: a review," *Wiley Journal Wireless Communications and Mobile Computing*, vol.2, issues 7, pp.653-666, 2002.

[5] D. Shiu, G. J. Foschini, M. J. Gans and J. M. Kahn, "Fading correlation and its effect on the capacity of multielement antenna systems,"*IEEE Transactions on Communications*, vol.48, no.3, pp.502-513, 2000.

[6] Ali Abdi, Mostafa Kaveh, "A Space-Time Correlation Model for Multielement Antenna Systems in Mobile Fading Channels," *IEEE J. on Selected Areas in Comms.*, vol.20, no.3, pp.550-560, April, 2002.

[7] B.T.Maharaj and L.P.Linde, "Capacity for Spatial-Temporal Correlated MIMO Fading Channel," *Proceedings of IEEE AFRICON*, vol 1, pp.269-274, September, 2004.

[8] G. J. Byers and F. Takawira, "The Influence of Spatial and Temporal Correlation on the Capacity of MIMO Channels," *in Proc.IEEE WCNC 2003*, vol.1, pp. 359-364, March, 2003.

[9] Latinovic. Z.; Abdi. A.; Bar-Ness. Y, "A Wideband Space-Time Model for MIMO Mobile Fading Channels," *Wireless Communications and Networking, IEEE*, Vol.1, pp.338-342, March, 2003.

[10] T. S. Rappaport, " Path loss exponents for different environments*," in Wireless Communications: principles and practice*, 2nd edition, Upper Saddle River, N. J: Prentice Hall PTR, 2002.

[11] J. Fuhl, A. F. Molisch and E. Bonek, "Unified channel model for mobile radio systems with smart antennas," *IEEE Proc. Radar, Sonar and Navigation*, vol.145, pp.32-41, February, 1998.

[12] W. C. Jakes Jr., "Multipath interference," *in Microwave Mobile Communications*, W. C. Jakes Jr., Ed. New York: Wiley, 1974.

[13] A. Abdi, J. A. Barger and M. Kaveh, "A parametric model for the distribution of the angle of arrival and the associated correlation function and power spectrum at the mobile station," *IEEE Trans. Veh. Technol.*, vol.51, pp.425-434, May, 2002.

[14] I. S. Gradshteyn and I. M. Ryzhik, M. Young, *Table of Integrals, Series, and Products*. 6 th Edition, A. Jeffery, Editor, San Diego, CA: Academic Press, ISBN 0 – 12 – 294757 – 6, 2000.

[15] B. Holter, "On the Capacity of the MIMO channel-A tutorial Introduction," *in Proc. Norwegian Signal Processing Conference*, Trodheim, Norway, October, 2001.

[16] Lee, W. C. Y., *Mobile Communications Engineering*, McGraw Hill Publications, New York, 1985.

[17] B.T. Maharaj, J.W. Wallace, L.P. Linde and M.A. Jensen, "A low cost open-hardware wideband MIMO wireless channel sounder", *IEEE Transactions on Instrumentation and Measurement*, vol. 57, no. 10 , pp. 2283-2289, October 2008.

Bobby. B. Varghese received his B.Eng degree in Electronics and Communication in 2001 from Kuvempu University, Karnataka, India. He has also received his B.Sc. Hons degree in Applied Science in 2003 from University of Pretoria, Pretoria, South Africa. He is currently working as a Voice Engineer at Saab Grintek Technologies (Pty) Ltd, South Africa and also worked part time towards his MSc degree in Applied Science at the University of Pretoria.
His current fields of interests are Wireless Communications, MIMO systems, Mobile technologies including UMTS and HSDPA and VoIP.

B.T. Maharaj (SMSAIEE, M MIET) received both his BSc Eng. and MSc Eng. in Electronic Engineering from University of Natal. He also holds a MSc in Operational Telecommunications (Merit) (1996) from University of Coventry, UK and a PhD from University of Pretoria.
He worked for Electromagnetic Laboratory (EMLAB) Pty Ltd and Grinaker Avitronics Ltd. as a microwave design engineer. He subsequently worked at the Eastern Cape Technikon and is currently a working in the Department of Electrical, Electronic and Computer Engineering, University of Pretoria, South Africa. His research interests are in MIMO wireless systems, channel modeling and as well as Cognitive Radio.